

# Structural insights into the mechanisms of urea permeation and distinct inhibition modes of urea transporters

Received: 28 March 2024

Accepted: 5 November 2024

Published online: 26 November 2024



Shen-Ming Huang<sup>1,2,10</sup>, Zhi-Zhen Huang<sup>3,10</sup>, Lei Liu<sup>2,4,10</sup>, Meng-Yao Xiong<sup>1,3,10</sup>, Chao Zhang<sup>5,10</sup>, Bo-Yang Cai<sup>1,10</sup>, Ming-Wei Wang<sup>2,10</sup>, Kui Cai<sup>1</sup>, Ying-Li Jia<sup>1</sup>, Jia-Le Wang<sup>1</sup>, Ming-Hui Zhang<sup>6</sup>, Yi-He Xie<sup>1</sup>, Min Li<sup>3</sup>, Hang Zhang<sup>1</sup>, Cheng-Hao Weng<sup>1</sup>, Xin Wen<sup>2</sup>, Zhi Li<sup>7</sup>, Ying Sun<sup>7</sup>, Fan Yi<sup>8</sup>, Zhao Yang<sup>5</sup>, Peng Xiao<sup>5</sup>, Fan Yang<sup>2,9</sup>, Xiao Yu<sup>9</sup>, Lu Tie<sup>3</sup>, Bao-Xue Yang<sup>3</sup> & Jin-Peng Sun<sup>1,2,5</sup>

Urea's transmembrane transport through urea transporters (UT) is a fundamental physiological behavior for life activities. Here, we present 11 cryo-EM structures of four UT members in resting states, urea transport states, or inactive states bound with synthetic competitive, uncompetitive or non-competitive inhibitor. Our results indicate that the binding of urea via a conserved urea recognition motif (URM) and the urea transport via H-bond transfer along the  $Q^{Pb}-T^{5b}-T^{5a}-Q^{Pa}$  motif among different UT members. Moreover, distinct binding modes of the competitive inhibitors 25a and ATB3, the uncompetitive inhibitor CF11 and the noncompetitive inhibitor HQA2 provide different mechanisms for blocking urea transport and achieved selectivity through L-P pocket, UCBP region and SCG pocket, respectively. In summary, our study not only allows structural understanding of urea transport via UTs but also afforded a structural landscape of hUT-A2 inhibition by competitive, uncompetitive and noncompetitive inhibitors, which may facilitate developing selective human UT-A inhibitors as a new class of salt-sparing diuretics.

Urea, one of the most ubiquitous organic compounds in nature, is the nitrogen source for many bacteria, a buffer that enables the survival of particular pathogens in acidic stomachs, and the final product of amino acid metabolism in the body of human and

animals<sup>1–3</sup>. Whereas rays and sharks use urea to sustain isosmotic activity against sea water, mammals normally concentrate urea up to hundreds of fold in the kidney to establish the osmotic gradient necessary for water reabsorption and urine concentration<sup>4–6</sup>.

<sup>1</sup>Department of Physiology and Pathophysiology, School of Basic Medical Sciences, State Key Laboratory of Vascular Homeostasis and Remodeling, Beijing Key Laboratory of Cardiovascular Receptors Research, Peking University, Beijing, China. <sup>2</sup>Advanced Medical Research Institute, Cheeloo College of Medicine, Shandong University, Jinan, Shandong, China. <sup>3</sup>Department of Pharmacology, School of Basic Medical Sciences, State Key Laboratory of Vascular Homeostasis and Remodeling, Peking University, Beijing, China. <sup>4</sup>The Second Hospital of Shandong University, Cheeloo College of Medicine, Shandong University, Jinan, China. <sup>5</sup>Key Laboratory Experimental Teratology of the Ministry of Education and Department of Biochemistry and Molecular Biology, School of Basic Medical Sciences, Cheeloo College of Medicine, Shandong University, Jinan, Shandong, China. <sup>6</sup>Department of General Surgery, Qilu Hospital of Shandong University, Jinan, Shandong, China. <sup>7</sup>Jiangsu Key Laboratory of New Drug Research and Clinical Pharmacy, Xuzhou Medical University, Xuzhou, Jiangsu, China. <sup>8</sup>The Key Laboratory of Infection and Immunity of Shandong Province, Department of Pharmacology, School of Basic Medical Sciences, Shandong University, Jinan, China. <sup>9</sup>Key Laboratory Experimental Teratology of the Ministry of Education and Department of Physiology, School of Basic Medical Sciences, Shandong University, Jinan, Shandong, China. <sup>10</sup>These authors contributed equally: Shen-Ming Huang, Zhi-Zhen Huang, Lei Liu, Meng-Yao Xiong, Chao Zhang, Bo-Yang Cai, Ming-Wei Wang. ✉e-mail: [tielu@bjmu.edu.cn](mailto:tielu@bjmu.edu.cn); [baoxue@bjmu.edu.cn](mailto:baoxue@bjmu.edu.cn); [sunjinpeng@sdu.edu.cn](mailto:sunjinpeng@sdu.edu.cn)

Moreover, urea nitrogen recycling plays key roles in the protein balance of mammals during hibernation<sup>7</sup>. Because urea has a stronger dipole moment than water, the free diffusion of urea across the plasma membrane is very slow. To facilitate urea transport in body, many organisms encode urea transporter (UT) genes, which are expressed as transmembrane proteins that play major roles in mediating the rapid transmembrane permeation of urea. The urea permeation rate of UTs is generally  $10^4 - 10^6$  urea molecules per second, which is 10 to 100 times higher than the rate of free diffusion. UTs play essential roles in balancing urea generation and excretion of normal physiological processing<sup>8</sup>.

Two subfamilies of UT have been found in mammals, UT-A and UT-B, which are encoded by the genes *Slc14a2* and *Slc14a1*, respectively. The *Slc14a2* gene of *Homo sapiens* produces four UT-A members, named hUT-A1 to -A3 and hUT-A6, by different promoters and alternative mRNA splicing (Fig. 1a and Supplementary Fig. 1a)<sup>9,10</sup>. UTs are expressed in various tissues throughout the human body. Four UT types, hUT-A1-A3 and hUT-B, play important roles in the urea recycling in the kidney, and hUT-A6 is expressed in human colon tissue. In addition, rat UT-A4 (rUT-A4) is found only in the renal medulla, while mouse UT-A5 (mUT-A5) is expressed only in the testis<sup>11</sup> (Fig. 1a). UT-A1 is the largest member in the UT family, consisting of 920 amino acids. UT-A2 consists of 396 amino acids that are the same as amino acids 524–920 of UT-A1. UT-A3 consists of amino acids 1–451 of UT-A1 (Supplementary Fig. 1a). UT-B shares 61.6% sequence similarity with UT-A2. In the kidney, UT-A1 and UT-A3 are expressed in the principal cells of the inner medullary collecting duct (IMCD), UT-A2 is expressed in the thin descending limb (TDL) of the loop of Henle, and UT-B is expressed in the renal descending vasa recta (DVR) (Fig. 1b). These four types of UT are responsible for the rapid urea recycling in the kidney<sup>12</sup>.

Functional abnormalities of UT are known to lead to abnormal distribution of urea in the body, causing urine concentrating defects, as well as affecting the cardiovascular and nervous systems, which may increase the cardiovascular burden and cause cognitive impairments<sup>13–15</sup>. The aberrant urea metabolism mediated by increased levels of UT could be one of the key elements of the neuropathogenesis of Huntington's disease<sup>16</sup>. Blocking UTs with inhibitors can inhibit the concentration of urine in the kidney and exert osmotic diuretic effect without affecting electrolyte excretion<sup>10</sup>, suggesting therapeutic potential as diuretics, which can be used for the long-term treatment of heart failure, edema, hypertension and so on<sup>17</sup>. However, the use of existing UT inhibitors as diuretics is hampered by their low affinity and poor selectivity, which can cause numerous side effects. Recently, the structures of a bacterial homolog UT and of bovine UT-B have been solved. Parallel to our work, the apo structures of human UT-A3 and UT-B and of UT-B bound with the selective inhibitor UTB<sub>inh</sub>-14, have been reported<sup>18</sup>. However, urea transport by UTs has not been directly observed, and the structural mechanisms that underlie urea transport and could enable the design of inhibitors targeting UT-A remain elusive. Notably, selective inhibitors targeting UT-A1-A3 are desired for diuretic usage instead of nonselective inhibitors or UT-B-selective inhibitors because UT-B is widely distributed throughout the body and UT-B inhibitors may therefore have side effects in nonrenal tissues<sup>10</sup>.

In this study, we present high-resolution structures of four apo UTs, human hUT-A2, hUT-A3, and hUT-B and zebrafish UT, as well as seven structures of these UTs in complex with urea, the competitive inhibitors 25a and ATB3, the uncompetitive inhibitor CF11 and the noncompetitive inhibitor HQA2. Combined with activity measurement, computational molecular dynamics (MD) simulation and mutational analysis, these structures provide important mechanistic insights into urea transport by UTs and selective competitive, uncompetitive or noncompetitive inhibitor designs targeting hUT-As.

## Results

### Expression and functional characterization of human UT

To facilitate the structural determination of UTs, we screened the plasma membrane expression levels of UT proteins. Flag tags were added to the N-termini of zebrafish UT (zf-UT) and human UT-A1, A2, A3, and UT-B sequences, and the mCherry protein was fused by the TEV cleavage site and GSA linker at the C-termini. zf-UT had the highest plasma membrane expression, followed by hUT-A2, hUT-A3 and hUT-B, whereas hUT-A1 showed no detectable expression in the insect cell membrane (Fig. 1c). Further examination of UT proteins by size exclusion column chromatography showed that the elution volumes of four highly expressed UT proteins (approximately 14.5 ml in Sepharose 6) were significantly earlier than those of the expected monomer proteins (approximately 17 ml), suggesting that these four UT proteins existed in the multimer forms (Fig. 1d and Supplementary Fig. 1b–d). Cross-linking with glutaraldehyde followed by gel electrophoresis suggested that the four highly expressed UT proteins all existed as trimers (Fig. 1e). These observations recalled previous reports of the trimer formation of *Desulfovibrio vulgaris* UT (dv-UT) and bovine UT-B<sup>19</sup>. Importantly, urea permeability, measured using the urease assay and <sup>14</sup>C-labeled urea transport assay, was significantly higher in HEK293 cells transfected with zf-UT, hUT-A2, hUT-A3, and hUT-B than in HEK293 cells transfected with the control pcDNA3.1 plasmid (Fig. 1f, g and Supplementary Fig. 1e, f). Moreover, the urea permeability of hUT-A2, hUT-A3, hUT-B, and zf-UT was blocked by the small-molecule inhibitor 25a (Fig. 1f, g).

### Overall cryo-EM structures of the UT trimers

We then determined nine structures of hUT-A2 and zf-UT in the resting state and bound to endogenous urea, the competitive inhibitor 25a or ATB3, the uncompetitive inhibitor CF11, or the noncompetitive inhibitor HQA2 via single-particle cryo-electron microscopy at resolutions ranging from 2.6 to 3.3 Å (Fig. 2a, d and Supplementary Figs. 2–5 and Supplementary Tables 1 and 2). The cryo-EM structures of hUT-A3 and hUT-B in the absence of urea were also solved at resolutions of 2.3 Å and 2.4 Å (Fig. 2b, c and Supplementary Fig. 4 and Supplementary Table 2). The cryo-EM densities allowed the assignment of most residues of the UT proteins, including residues 51 to 381 of hUT-A2, residues 96 to 440 of hUT-A3, residues 34 to 383 of hUT-B and residues 31 to 380 of zf-UT (Supplementary Table 3). The density of urea and inhibitors could also be assigned in the hUT-A2 and zf-UT structures in either intracellular or extracellular regions of the transport channels (Fig. 2a, d).

Consistent with the electrophoresis results, zf-UT, hUT-A2, hUT-A3 and hUT-B all existed as homologous trimers in the solved cryo-EM structures (Fig. 2 and Supplementary Fig. 6a–d). In all these UT structures, each UT unit consists of 10 complete transmembrane helices and 2 semi-transmembrane helices distributed symmetrically along the axis of the urea transport channel, which were named 1a–5a, 1b–5b, and Pa, and Pb, respectively (Supplementary Fig. 6e). The two symmetric halves of each UT subunit are named the a-half and b-half, respectively, and are connected by a long extracellular loop (LECL) (Supplementary Fig. 6e). The urea transport channels of all UTs are enclosed by helices from both halves, including helices 3a, 3b, 5a, 5b, Pa, and Pb (Fig. 3a and Supplementary Fig. 6a–e)<sup>19</sup>. Both the N-terminus and C-terminus of each UT subunit face the intracellular side. A portion of the C-terminus of UT folds into a helical-like structure and is named the C1 helix. Between the C1 helix and helix 5b is the long intracellular loop (LICL), which is also located on the cytoplasmic side (Supplementary Fig. 6e).

Importantly, most structural differences between different UTs are located in the N-terminus, C-terminus, LECL and long intracellular loop (LICL). Compared with the structure of hUT-A2, the N-terminus of hUT-A3 has an extra  $\alpha$  helix, named the N1 helix. The C1 helix of hUT-A3 is one helical turn shorter than the C1 helix of hUT-A2 and is rotated

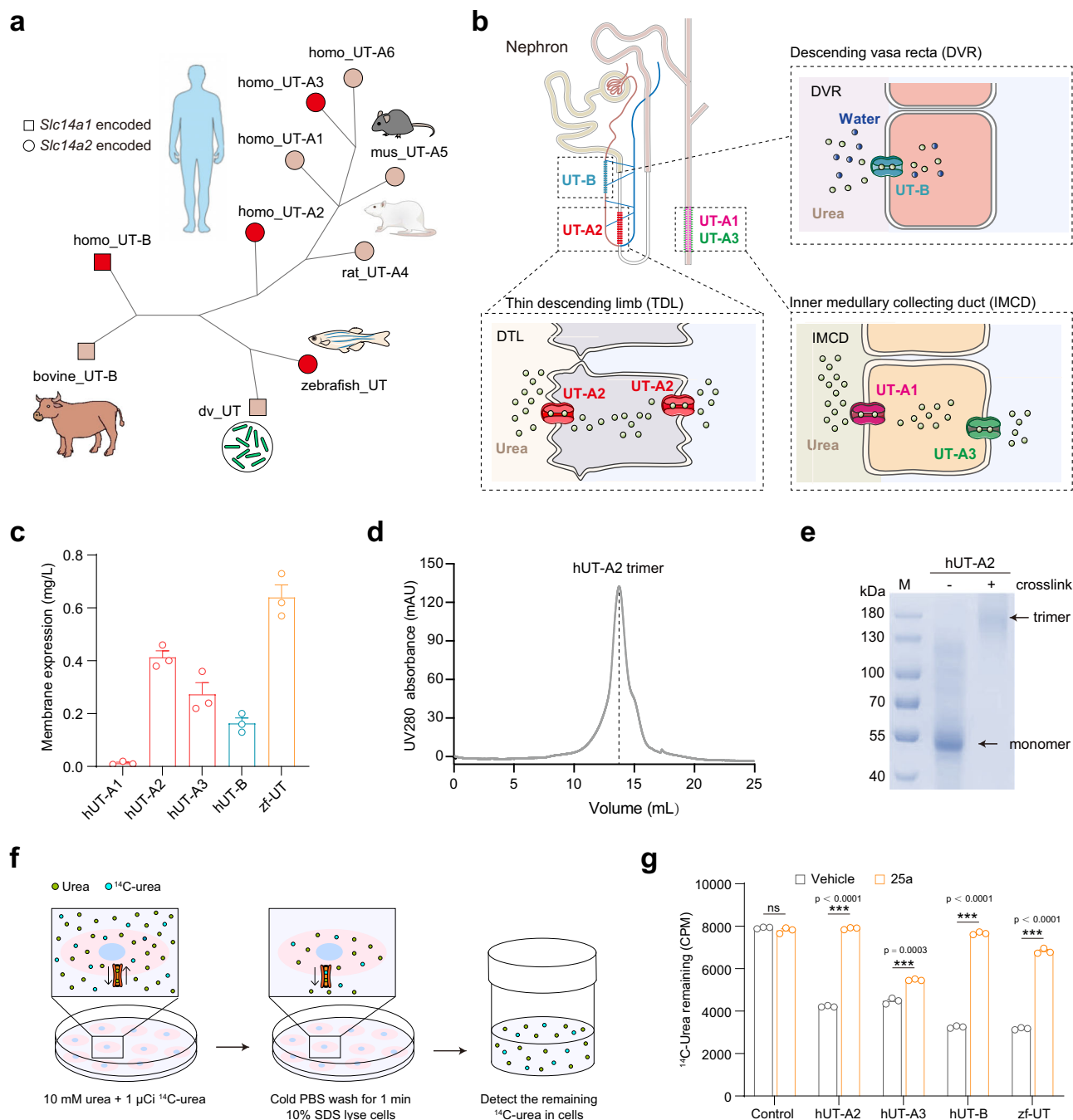


**Fig. 1 | Expression and functional characterization of the urea transporters.**

**a** The dendrogram clustering representation of the evolutionary relationship of UTs from different species, including human, bovine, mouse, rat, zebrafish and *Desulfovibrio vulgaris* (dv\_UT). Five UT members are expressed in human, containing UT-B and four UT-As. The squares and the circles represent UTs encoded by gene *Slc14a1* and *Slc14a2*, respectively. The UTs whose structure were determined in our paper are highlighted with red color. dv, *Desulfovibrio vulgaris*. **b** Tissue distribution of UT expressed in the human kidneys. UT-A1 and UT-A3 are expressed in the principal cells of the inner medullary collecting duct (IMCD), UT-A2 is expressed in the thin descending limb (TDL) of the loop of Henle, and UT-B is expressed in the renal descending vasa recta (DVR). **c** The membrane expression levels of the human UT-A1-A3, UT-B and zf-UT, which were overexpressed in SF9 cells using a Bac-to-Bac baculovirus expression system. Data are represented as mean  $\pm$  SEM from 3 independent experiments ( $n = 3$ ). **d** The size-exclusion chromatography elution profiles

of the purified hUT-A2 on Superose 6 Increase 10/300 column. The peak of hUT-A2 was approximately 14.5 ml. **e** Representative SDS-PAGE results of the purified hUT-A2 ( $n = 2$ ). After cross-linking with glutaraldehyde, the hUT-A2 showed at a size corresponding to trimer form displayed on the SDS-PAGE. **f** Schematic diagram of the  $^{14}\text{C}$ -labeled urea transportation assay. Each cell well was incubated with 300  $\mu\text{l}$  of DMEM supplemented with 10 mmol/L urea and 1  $\mu\text{Ci}$  of  $^{14}\text{C}$ -urea for 30 min. After incubation, the cells were washed with cold 1xPBS. Then, the cells were lysed and transferred into 5 ml of scintillation fluid in a scintillation vial for measured by using a scintillation counter. The detailed experimental procedures are shown in the Methods section. **g** Urea permeability shown by the detection of remaining  $^{14}\text{C}$ -labeled urea. Columns of cells treated with vehicle or 100  $\mu\text{M}$  inhibitor 25a are colored gray or orange respectively. Data are represented as mean  $\pm$  SEM from 3 independent experiments ( $n = 3$ ). \*\*\* $P < 0.001$ , statistical differences were determined by the two-sided unpaired Student's *t*-test (compared with vehicle).

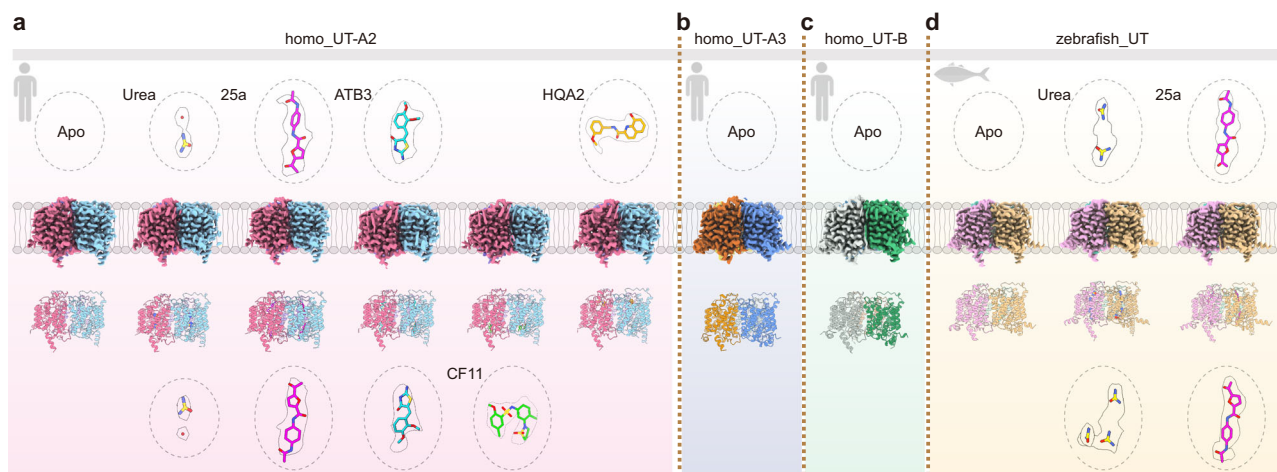


**Fig. 2 | Cryo-EM structures of hUT-A2, hUT-A3, hUT-B and zf-UT. a–d** Overall cryo-EM densities and structures of hUT-A2 (a), hUT-A3 (b), hUT-B (c) and zf-UT (d) homotrimer. The cryo-EM densities of different UTs are displayed on the phospholipid bilayer cell membrane with the represent cartoon models shown below.

Molecules bound to the extracellular and intracellular sides of different UTs, along with their corresponding EM densities, are indicated in dashed circles at the top and bottom layers, respectively. Created in BioRender. Huang, S. (2024) <https://BioRender.com/h99o001>.

outward by approximately 8° (Supplementary Fig. 6f). Compared with hUT-A2, the N-terminus of hUT-B has two more helical structures, which are named N1 and N2. The C1 helix of UT-B is rotated outward by approximately 11°, and the intracellular ends of helix 4a, LECL and LICL are shifted inward compared with the corresponding positions in UT-A2 (Supplementary Fig. 6g). The N-terminus of zf-UT is similar to the N-terminus of hUT-B, with two helices, N1 and the N2. Compared to hUT-A2, the C1 helix of zf-UT is rotated outward by approximately 6°, and the LECL and LICL are shifted inward (Supplementary Fig. 6h).

### Capture of urea in the urea transport channel

In the hUT-A2 structure, the urea transport channel connecting the extracellular section to the intracellular region is composed of helices 3a, 3b, 5a, 5b, Pa, and Pb. The channel is a continuous cavity that is wide at both ends and narrow in the middle, with a length of approximately 21 Å (Fig. 3a). Compared with the apo-hUT-A2 structure, the additional EM density in this potential urea transport channel at the 4.0  $\sigma$  contour level enabled us to model the urea molecule and its coupled water on both the extracellular and cytoplasmic sides (Fig. 3b and Supplementary Fig. 7a, b). The modeled urea molecules were further supported by molecular dynamics simulation (Supplementary Fig. 7c). There are two urea binding pockets in the channel: one in the extracellular urea binding pocket (EUBP) and the other in the cytoplasmic urea binding pocket (CUBP), separated by approximately 10 Å (Fig. 3c–e). In total, 7 residues compose the EUBP, and the largely hydrophobic environment is decorated with many polar groups. In the EUBP, two nitrogen atoms of the upper urea form a salt bridge with the main chain carbonyl oxygens of Q231<sup>Pb</sup> and V232<sup>Pb</sup>, a hydrogen bond with the side chain of T338<sup>Sb</sup> and a water-mediated hydrogen bond with the side chain of Q231<sup>Pb</sup> (Fig. 3d). In addition to polar interactions, urea molecules form a cation- $\pi$  interaction with the benzene ring of F287<sup>Sb</sup> and van der Waals interactions with L131<sup>3a</sup>, F179<sup>5a</sup>, and C337<sup>Sb</sup> (Fig. 3d).

The CUBP consists of 5 hydrophobic residues and 2 polar residues (Fig. 3e). Notably, the lower urea molecule in the CUBP form symmetric polar interactions and hydrophobic packing compared with the upper urea molecule in the EUBP, including interactions with the main chain carbonyl groups of Q67<sup>Pa</sup> and V68<sup>Pa</sup> and the side chain of T176<sup>5a</sup>, as well as cation- $\pi$  interactions with F70<sup>Pa</sup> and Y123<sup>3a</sup> (Fig. 3e). The motif Q67<sup>Pa</sup>V68<sup>Pa</sup>Y123<sup>3a</sup>T176<sup>5a</sup> in the CUBP and the motif Q231<sup>Pb</sup>V1232<sup>Pb</sup>F/Y287<sup>Sb</sup>T338<sup>Sb</sup> in the EUBP are conserved among UT-

A2, UT-A3, UT-B and zf-UT and thus could be a “urea recognition motif (URM)” in UTs (Fig. 3f). In addition, the lower urea molecule in the CUBP forms contacts with F175<sup>5a</sup> and F341<sup>Sb</sup> (Fig. 3e). Consistent with these observations, alanine mutations of the residues in the URM of either the CUBP or the EUBP, such as Y123<sup>3a</sup> and T176<sup>5a</sup> in the CUBP or Q231<sup>Pb</sup> F/Y287<sup>Sb</sup> and T338<sup>Sb</sup> in the EUBP significantly decreased urea transport by these UTs (Fig. 3g, h and Supplementary Fig. 7d–g).

### Potential urea permeation mechanism of the human urea transporter hUT-A2

Compared with that of apo-hUT-A2, the pore size of the urea transport channel of urea-bound hUT-A2 is significantly smaller, and the mean radius is decreased by approximately 0.3 Å (Fig. 4a and Supplementary Fig. 7h). The shrinkage of the channel radius is mainly due to the inward movements of residues such as F70<sup>Pa</sup>, Y123<sup>3a</sup>, L127<sup>3a</sup>, L131<sup>3a</sup>, F179<sup>5a</sup> and F287<sup>Sb</sup> (Supplementary Fig. 7i). We speculated that the hydrogen bonding and hydrophobic interactions of urea in the urea transport channel are the driving forces for channel cavity shrinkage and the resulting smaller radius (Fig. 4b). The UT transport channels are divided into three parts, So, Sm, and Si, from the extracellular to the cytoplasmic side. In the So region, the urea molecule forms a salt bridge with the main chain oxygen atoms of Q231<sup>Pb</sup> and V232<sup>Pb</sup> and a hydrogen bond with the hydroxyl group of T338<sup>Sb</sup> (Fig. 4b). The hydrophobic side chains of L131<sup>3a</sup> and F287<sup>Sb</sup> provide steric hindrance for the orientation of the urea molecule. These interactions induce the inward movements of several residues inside the transport channel, such as L127<sup>3a</sup>, L131<sup>3a</sup>, and F179<sup>5a</sup>, as well as F287<sup>Sb</sup> on the other side (Supplementary Fig. 7i).

The urea molecule in the Si region shows a similar symmetric bonding pattern. The Sm region of the UT transport channel is a relatively narrow cavity consisting of three residue pairs, namely, T176<sup>5a</sup>–T338<sup>Sb</sup>, L127<sup>3a</sup>–L291<sup>3b</sup>, and F179<sup>5a</sup>–F341<sup>Sb</sup> (Fig. 4b). The pore radius of this central core of the Sm region is significantly smaller than that of the So and Si regions (Supplementary Fig. 7h). Because our current cryo-EM data of urea-hUT-A2 could not capture clear EM density inside the Sm region, we performed MD simulation to explore the process of urea molecule passing through the Sm region (Supplementary Fig. 7j). The simulation captured three low-energy states with longer residence times of urea across the channel, located in the three defined regions, So, Sm, and Si, with distribution probabilities of time of 37%, 19% and 34%, respectively (Fig. 4c–e). According to kinetic



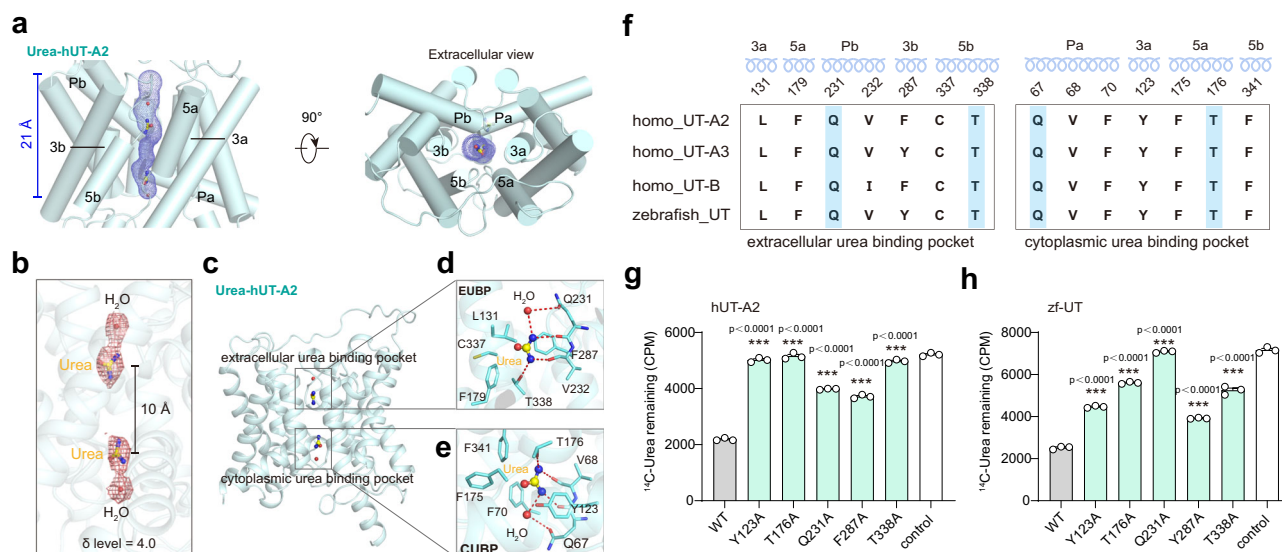


**Fig. 3 | Visualize the urea transportation across the channel of hUT-A2.** **a** The urea transport channel of hUT-A2 is shown as blue dots with the surrounding helices displayed as cylinders. The urea transport channel of hUT-A2 is a continuous cavity with a length of approximately 21 Å which is enclosed by helices from both halves, including helices 3a, 3b, 5a, 5b, Pa, and Pb. **b** The EM density in the urea binding pocket of hUT-A2 at the 4.0  $\sigma$  contour level are shown as red mesh on both the extracellular and cytoplasmic sides of the urea transport channel. **c** The extracellular urea binding pocket (EUBP) and the cytoplasmic urea binding pocket (CUBP) of hUT-A2. **d, e.** The key residues interacting with urea in EUBP (**d**) and CUBP (**e**) are shown as sticks while the urea and water molecules are displayed as stick-balls and red balls, respectively. The H-bonds are shown as red dashed lines.

**f** Structurally equivalent residues in the EUBP (left) and CUBP (right) of hUT-A2 compared with other hUTs and zf-UT. The secondary structure of the indicated residues is shown at the top. The conserved Q<sup>Pb</sup>-T<sup>5b</sup>-T<sup>5a</sup>-Q<sup>Pa</sup> motif of urea transport channel in different UTs is shown in blue backgrounds. **g, h** Urea permeability shown by the detection of remaining <sup>14</sup>C-labeled urea in cell transfected with hUT-A2 (**g**) and zf-UT (**h**). Cells transfected with wild type and mutant UT plasmids are shown as gray and green columns respectively, while cells transfected with pcDNA3.1 blank plasmids for control are shown as blank column. Data are represented as mean  $\pm$  SEM from 3 independent experiments ( $n = 3$ ). \*\*\* $P < 0.001$ , statistical differences were determined by the two-sided unpaired Student's *t*-test (compared with wild type).

simulation and cluster analysis, the side chains of T176<sup>5a</sup> and T338<sup>5b</sup> rotated by approximately 40° followed by the rearrangement of the side chains of T176<sup>5a</sup>-T338<sup>5b</sup> and F179<sup>3a</sup>-F341<sup>3b</sup> to allow the urea molecule to pass through the Sm region. In the Sm region, the oxygen atom of urea formed hydrogen bonds with the hydroxyl group of the T176<sup>5a</sup>-T338<sup>5b</sup>, while the nitrogen atom formed hydrogen bonds with the main chain carbonyl group of V68<sup>Pa</sup>-V232<sup>Pb</sup> (Fig. 4f, g). Moreover, the polar urea molecules also interacted with the hydrophobic side chains of T338<sup>5b</sup>/T176<sup>5a</sup>, V232<sup>Pb</sup>/V68<sup>Pa</sup> and L127<sup>3a</sup>/L291<sup>3b</sup> through van der Waals forces in the Sm region (Fig. 4g, h). The urea molecules were sterically restricted by the side chains of amino acids L127<sup>3a</sup>-L291<sup>3b</sup> and F179<sup>3a</sup>-F341<sup>3b</sup> in the Sm region (Fig. 4h). Therefore, urea molecules shuttle through the transport channel in the form of a “monolith”, supporting a previous hypothesis<sup>1,19</sup>. We speculated that the urea molecule rotated via H-bond formation with the Q231<sup>Pb</sup>-T338<sup>5b</sup>-T176<sup>5a</sup>-Q67<sup>Pa</sup> motif during transportation (Supplementary Movie). Consistent with these simulation results and our hypothesis, the mutations Q67A, T176A, Q231A and T338A etc. of hUT-A2 significantly impaired urea permeation efficiency (Figs. 3g, 4i and Supplementary Fig. 7k, l).

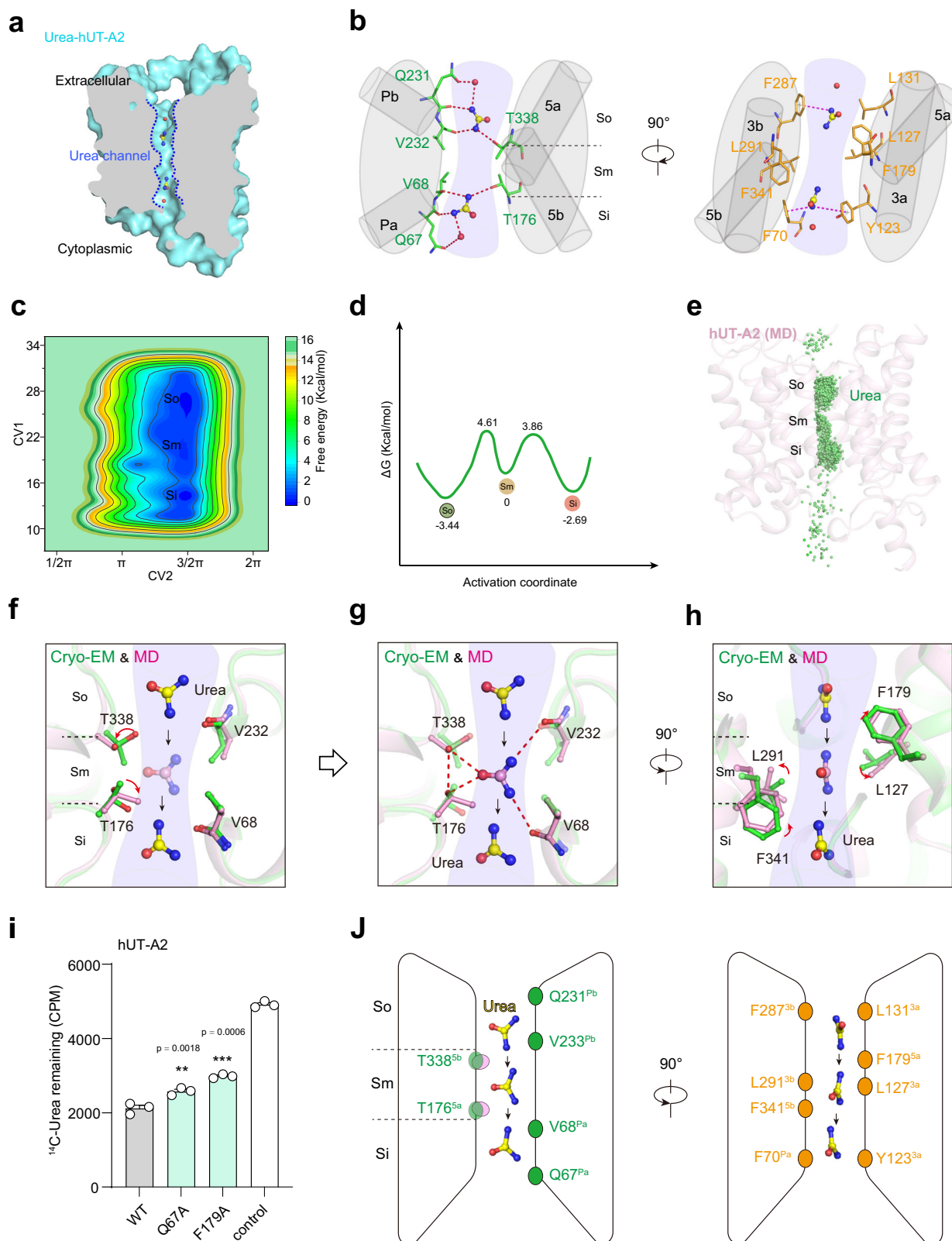
We therefore hypothesized that the transport of urea across hUT-A2 occurs in three steps. In the first step, free urea molecules in solution are captured by the flexible side chain of Q231<sup>Pb</sup> in the extracellular region. The urea molecules are then brought into the So region of the transport channel by the rotation of the side chain of Q231<sup>Pb</sup> and coordinated by water molecules. At this stage, the two basic nitrogen atoms of the urea molecule form a salt bridge with the negatively charged poles of the Pa helix backbone (carbonyl oxygen atoms of the Q231<sup>Pb</sup> and V232<sup>Pb</sup> main chains). The hydrophobic nature of L131<sup>3a</sup>-F287<sup>3b</sup> facilitates a defined orientation of the urea molecule on the horizontal plane. In the second step, the flexibility of the side chains of L131<sup>3a</sup> and F287<sup>3b</sup> and hydrogen bond transfer mediated by the side chain of T338<sup>5b</sup> pull the urea molecules into the Sm region. In particular,

rearrangement of the configurations of the residue pairs L127<sup>3a</sup>-L291<sup>3b</sup> and F179<sup>3a</sup>-F341<sup>3b</sup> may allow the entry of urea molecules. In the third step, the movement of the T176<sup>5a</sup> side chain may transfer the urea molecules from the Sm region to the Si region, forming an interaction pattern that is symmetric to the interaction pattern of urea in the So region (Fig. 4j). The urea may then move downward to form a hydrogen bond with the side chain of Q67<sup>Pa</sup>. Finally, the urea bound to the Si region is released into the cytoplasm, thus completing the transport of urea from the extracellular to the intracellular space. We speculated that the formation and transfer of hydrogen bonds between urea and the Q231<sup>Pb</sup>-T338<sup>5b</sup>-T176<sup>5a</sup>-Q67<sup>Pa</sup> motif play important roles throughout the whole process of urea transport (Fig. 4j). Because the distribution of amino acids in the So and Si regions of the channels is relatively symmetrical, we speculated that urea molecules can be transported from the intracellular end to the extracellular end in a similar manner (Fig. 3f).

### Observation of urea transport by zf-UT

The trimer structure of urea-bound zf-UT was solved at an overall resolution of 3.0 Å. Compared with the apo-zf-UT structure, obvious and continuous EM densities enabled easy assignment of urea on both the intracellular and extracellular sides of the zf-UT channel (Figs. 2d, 5a, b and Supplementary Fig. 8a–c). According to the EM density distribution, the urea transport channel contains a vertical tubular cavity composed of 3a, 3b, 5a, 5b, Pa, and Pb helices and then extends into the intracellular section composed of the intracellular ends of helices 3a–5a and ICL2b (Fig. 5c). Due to the continuous EM density, MD simulations were performed to model urea at specific positions of the urea transport channel (Fig. 5d–f).

Compared with the cryo-EM structure of urea-hUT-A2, the structure of urea-zf-UT has additional EM density connected to the “So” region on the extracellular side, which is named the “So” region, a cavity created by the side chains of F135<sup>3a</sup>, L284<sup>3b</sup>, and P335<sup>ECL2b</sup> (Fig. 5f and Supplementary Fig. 8b–e). Our MD simulation indicated that F135<sup>3a</sup> and



L284<sup>3b</sup> form transient interactions with urea during urea transport (Fig. 5f–h). The conservation of F135<sup>3a</sup> and L284<sup>3b</sup> among UTs of different species suggested that the channel governed by these two residues is a common path for urea transport (Fig. 5i). On the intracellular side, the EM density of zf-UT-urea enabled the identification of two other urea binding sites, which were named Si' and Si'', connecting to the Si region via an “L” configuration (Fig. 5b, f, h and Supplementary

Fig. 8c). Whereas urea in the Si' region contacts F300<sup>3b</sup> and L363<sup>1CL2b</sup>, urea in the Si'' region interacts with Y121<sup>3a</sup> and S160<sup>4a</sup> (Fig. 5h and Supplementary Fig. 8c). We noticed that key residues in the urea transport channel, such as Y287<sup>3b</sup>, L120<sup>3a</sup>, and Y121<sup>3a</sup> of zf-UT, were replaced by F, F, and H, respectively (Fig. 5i). These amino acid differences may contribute to the stronger and longer EM density of urea observed in the zf-UT-urea compared with that in the hUT-A2-urea complex structure.

**Fig. 4 | Urea permeation mechanism of the human urea transporter hUT-A2.** **a** The urea transport channel of hUT-A2 is highlighted by blue dotted line with the inner urea molecules displayed as stick-balls. **b** The hydrogen bonding and hydrophobic interactions of urea in the urea transport channel of hUT-A2. The black dashed lines are used to separate So, Sm, and Si regions of the channel. The H-bond are shown as red dashed line and the cation- $\pi$  interaction are shown as purple dashed lines. **c** Free energy surface (FES) of urea within the hUT-A2 channel. The simulation reveals three distinct low-energy states, which are characterized by prolonged urea residence times across defined regions within the channel and corresponds to the So, Sm, and Si regions respectively. **d** Simplified one-dimensional energy landscape highlighting the So, Sm, and Si states of urea within the hUT-A2 channel. **e** Metadynamics analysis depicts urea dynamically transitioning between three states-So, Sm, and Si-within the hUT-A2 channel, with distribution probabilities of 37%, 19%, and 34%, respectively. **f–h** Metadynamics simulations elucidate the passage of urea through the Sm region. This process

involves a rotation of approximately 40° in the side chains of T176<sup>5a</sup> and T338<sup>5b</sup>, facilitating the rearrangement of T176<sup>5a</sup>–T338<sup>5b</sup> side chains (**f**). Notably, hydrogen bond formations between urea and specific residues, including T338<sup>5b</sup> and T176<sup>5a</sup>, are depicted (**g**). The rotation of side chains of T338/T176 and structural rearrangement of L127/L291 form a hydrophobic cavity in the Sm region, guiding urea transportation across the channel (**h**). The H-bond are shown as red dashed line. The blue arrows indicate the direction of movement of the urea molecule. **i** Urea permeability shown by the detection of remaining <sup>14</sup>C-labeled urea in cell transfected with different hUT-A2. plasmids are shown as gray and green columns respectively, while cells transfected with pcDNA3.1 blank plasmids for control are shown as blank column. Data are represented as mean  $\pm$  SEM from 3 independent experiments ( $n = 3$ ). \*\* $P < 0.01$ , \*\*\* $P < 0.001$ , statistical differences were determined by the two-sided unpaired Student's  $t$ -test (compared with wild type). **j** Schematic diagram of urea permeation mechanism of hUT-A2.

In the So and Si regions of the channel, urea showed similar interaction modes to those in the urea-hUT-A2- structure, including the polar network constituted by the Q231<sup>Pb</sup>–T338<sup>5b</sup>–T176<sup>5a</sup>–Q67<sup>Pa</sup> motif and hydrophobic interactions involving L131<sup>3a</sup>, F287<sup>3b</sup>, F70<sup>Pa</sup>, and Y123<sup>3a</sup>, which are distributed along the channel from the extracellular side to the intracellular side (Fig. 5i). These results indicate that a common mechanism and conserved motifs underlie urea transport in UTs from different species.

### Competitive inhibition of UT-A2 by 25a

25a is a synthetic competitive inhibitor of UT with potency in the micromolar range ( $IC_{50} = 0.58 \pm 0.01 \mu M$  toward hUT-A2) (Fig. 6a and Supplementary Fig. 9a, Supplementary Table 4). We solved the cryo-EM structure of hUT-A2 with 25a to understand the structural basis of its inhibition and to facilitate more potent and selective UT inhibitor design. Unambiguous EM density corresponding to 25a could be easily assigned on both the extracellular and intracellular sides (Figs. 2a, 6b and Supplementary Fig. 9b). The furan group of 25a, which mimics the urea molecule, inserts deeply into the channel center and occupies the pocket region of the EUBP and CUBP (Fig. 6c–f and Supplementary Fig. 9c–f, Supplementary Table 5). On the extracellular side, the methyl ketone group and amide group on the two sides of furan form hydrogen bonds with the side chains of T338 and Q231 (Fig. 6c, e). In addition to polar interactions, the furan group of 25a undergoes hydrophobic packing with residues in the EUBP, such as L131<sup>3a</sup>, F179<sup>5a</sup>, V232<sup>3b</sup>, F287<sup>3b</sup>, and C337<sup>3b</sup>. On the cytoplasmic side, the furan ring of 25a forms similar interactions in a symmetric manner (Fig. 6c, e).

Notably, in addition to interacting with residues of the EUBP and CUBP, 25a occupies two additional pockets on the extracellular side and intracellular side, which are named the extracellular blocker binding pocket 1 (EBBP1) and the cytoplasmic blocker binding pocket 1 (CBBP1) (Fig. 6e, f). The EBBP consists of residues from helices 3a and 3b–4b, the LECL, and the ECL2b, and the CBBP consists of residues from helices 3a and 3b, the ICL2a, and the LICL (Supplementary Fig. 9e, f). The benzene ring structure of 25a forms  $\pi$ - $\pi$  stacking interactions with F135<sup>3a</sup> of the EBBP on the extracellular side or F120<sup>3a</sup>, and F300<sup>3b</sup> of CBBP on the intracellular side (Fig. 6c–f). The terminal end of 25a reached L202<sup>LECL</sup>, A326<sup>4b</sup> and P336<sup>ECL2b</sup> at the pocket end of the EBBP on the extracellular side but reached a relatively open space by contacting L363<sup>LICL</sup> of CBBP on the intracellular side (Fig. 6c–f). Consistent with these observations, the mutations F120L, F120V, and L202V diminished the binding of hUT-A2 with 25a (Fig. 6g–j and Supplementary Fig. 9g, h).

Collectively, these structural and mutational analyses indicated that the urea channel blocker 25a, by binding to both ends of the transmembrane transport channel (EUBP and CUBP), competes with urea to form hydrogen bonds with the conserved Q<sup>Pb</sup>–T<sup>5b</sup>–T<sup>5a</sup>–Q<sup>Pa</sup> motif necessary for urea transport (Fig. 3f), thereby competitively inhibiting the activity of UT.

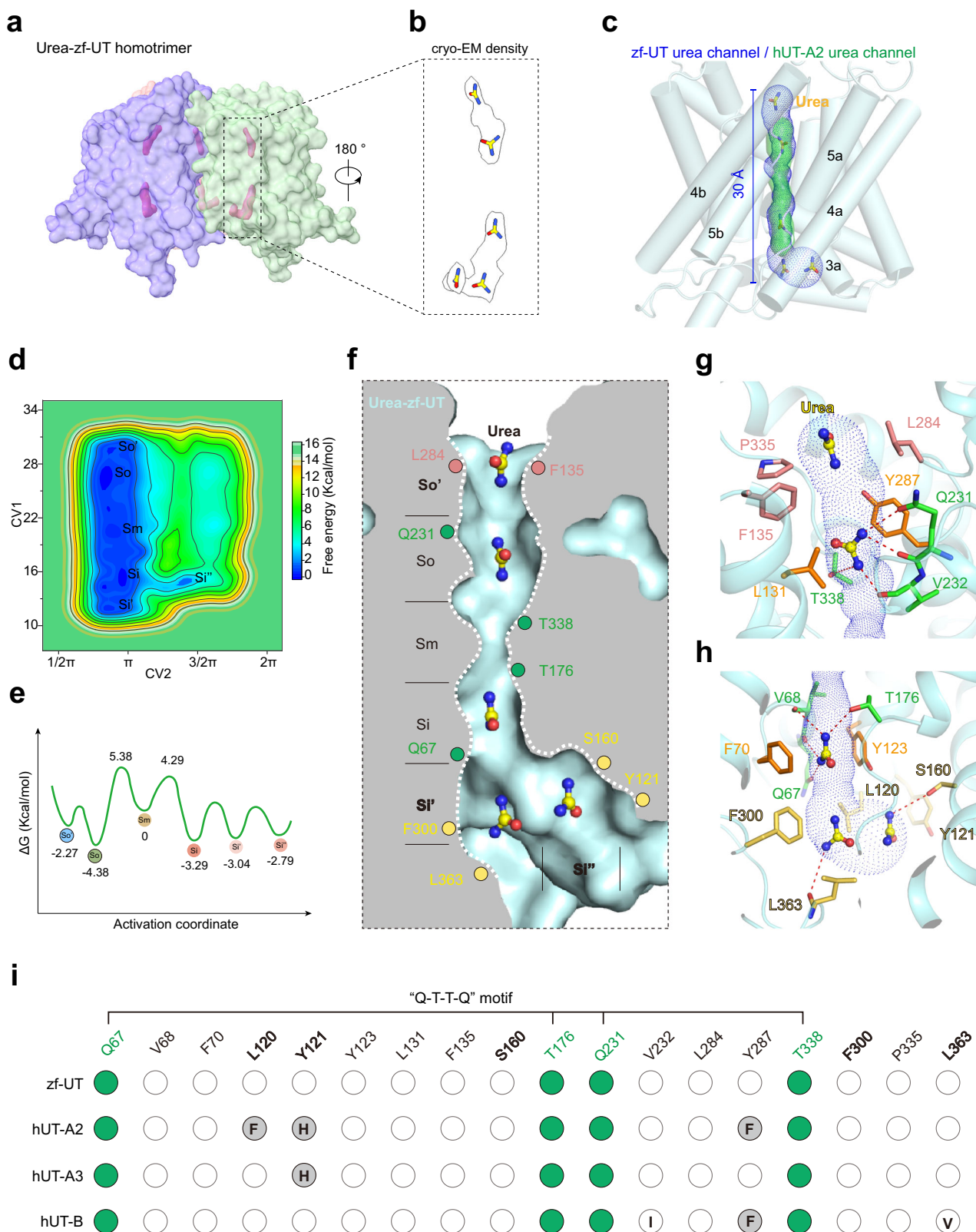
### Potential of selective UT-A inhibitor design by targeting the EBBP and CBBP

Synthetic compounds with selective activities for UT-A blockade could be used as urea diuretics where conventional salt-transporter blocking diuretics are limited. We next analyzed whether the structure of 25a-hUT-A2 provided clues for selective UT-A inhibitor design. Structural comparison suggested that the amino acids of L202<sup>LECL</sup> and P336<sup>ECL2a</sup> of the EBBP in hUT-A2 are replaced by V203<sup>LECL</sup> and A337<sup>ECL2a</sup> in hUT-B (Fig. 6g, h), decreasing the hydrophobic volume of the side chains. Molecular dynamics simulation suggests that these changes weaken the hydrophobic interaction between 25a and UT-B (Supplementary Fig. 9i). On the cytoplasmic side, F120<sup>3a</sup> of the CBBP of hUT-A2 is replaced by L121<sup>3a</sup> in UT-B (Fig. 6g), which disrupts  $\pi$ - $\pi$  interactions with the benzene ring of 25a and thus may decrease its binding affinity with UTs. Consistently, the mutations L202V and F120L of hUT-A2 significantly decreased the  $IC_{50}$  of 25a ( $L202V-IC_{50} = 3.41 \pm 0.01 \mu M$ ;  $F120L-IC_{50} = 1.65 \pm 0.02 \mu M$ ) (Fig. 6i, j). These results indicate that the selective residue differences in the EBBP and CBBP of UT, such as the nonconserved F120<sup>3a</sup> and L202<sup>LECL</sup>, could be exploited for selective and potent hUT-A2 inhibitor design (Fig. 6h).

### Structural basis of the selective inhibition of UT-A by ATB3

The aminothiazolone derivative UTA<sub>inh</sub>-B3 (ATB3) is a competitive inhibitor of hUT-A2 ( $IC_{50} = 6.38 \pm 0.54 \mu M$  toward UT-A2), showing approximately 6-fold stronger inhibition potency toward UT-B (Fig. 7a and Supplementary Table 4). To understand the mechanism underlying the selective inhibition of hUT-A2 by ATB3, we solved the cryo-EM structure of ATB3-hUT-A2 at an overall resolution of 3.3 Å (Supplementary Fig. 3a–f). EM densities corresponding to ATB3 were unambiguously detected on both the extracellular and intracellular sides (Figs. 2a, 7b–d and Supplementary Fig. 10a, b). On the extracellular side, the phenyl ring of ATB3 is rotated toward the channel axis by approximately 50°, and the thiazole heterocycle is shifted upward by approximately 1.5 Å compared with 25a (Fig. 7e). This difference in position enables the contact of ATB3 with F282<sup>3b</sup> in EBBP2 (constituted by F135<sup>3a</sup>, L202<sup>LECL</sup>, F282<sup>3b</sup>, and L284<sup>3b</sup>), which does not interact with 25a in the 25a-hUT-A2 complex structure (Fig. 7c, e, f and Supplementary Table 6). Specifically, ATB3 forms both polar and hydrophobic interactions with hUT-A2. In the EUBP, the nitrogen atoms and carbonyl group of the thiazole ring of ATB3 form hydrogen bonds and polar interactions with Q231<sup>Pb</sup> and T338<sup>5b</sup> (Fig. 7c, f). Whereas the ortho-methoxy group of ATB3 forms hydrophobic interactions with L284<sup>3b</sup> and P336<sup>ECL2b</sup> in EBBP1, the benzene ring and the meta-methoxy group form  $\pi$ - $\pi$  stacking and hydrophobic interactions with F135<sup>3a</sup>, L202<sup>LECL</sup>, F282<sup>3b</sup>, and L284<sup>3b</sup> in EBBP2 (Fig. 7c, f). On the cytoplasmic side, the thiazole ring is shifted by 1.5 Å away from the Sm region of the channel and forms polar interactions with Q67<sup>Pa</sup> and T176<sup>5a</sup> in the CUBP (Fig. 7d and Supplementary Fig. 10c, d). Notably, the thiazole ring of ATB3 forms





extensive polar interactions with the "Q<sup>Pb</sup>-T<sup>Pb</sup>-T<sup>3a</sup>-Q<sup>Pa</sup>" motif of the UT channel, which is essential for UT transport. We speculated that competing with urea for interactions with the "Q<sup>Pb</sup>-T<sup>Pb</sup>-T<sup>3a</sup>-Q<sup>Pa</sup>" motif underlies the inhibition mechanism of the UT inhibitor ATB3 (Fig. 7c, d and Supplementary Fig. 10d, Supplementary Table 6). Importantly, two specific residues interacting with methoxy groups

of ATB3, L202<sup>LECL</sup> and P336<sup>ECL2b</sup>, are replaced by V203<sup>LECL</sup> and A337<sup>ECL2b</sup> in UTB, respectively (Fig. 7g-i). MD simulation and mutational analysis indicated that these amino acids differences in structurally equivalent residues at the L202<sup>LECL</sup>-P336<sup>ECL2b</sup> motif ("LP" pocket) contribute to the selective inhibition of hUT-A2 by ATB3 compared with UTB (Fig. 7j-l and Supplementary Fig. 9g, h).



**Fig. 5 | Structural analysis and comparison of urea transport in zf-UT and hUTs.** **a, b** Overall view of the urea density in zf-UT trimer. Two portions of obvious and continuous cryo-EM densities corresponding to urea in zf-UT are located at both the intracellular and extracellular sides of the channel (**a**), which facilitated the unambiguous assignment of urea molecules (**b**). **c** Comparison of the transportation channel of zf-UT (blue) and hUT-A2 (green). According to the EM density distribution, the urea transportation channel of zf-UT contained a vertical tubular cavity composed by 3a, 3b, 5a, 5b, Pa, and Pb helices, and then extends into the intracellular section composed by intracellular ends of helices 3a–5a and ICL2b. **d** Free energy surface (FES) of urea across the zf-UT channel, revealing six low-energy states—So', So, Sm, Si, Si', and Si''—associated with extended urea residence times across six distinct regions within the channel. **e** Simplified one-dimensional energy landscape illustrating the So', So, Sm, Si, Si', and Si'' states of urea within the zf-UT channel. **f** The location of the urea molecules are modeled into six regions

shown as So', So, Sm, Si, Si', and Si'' in the zf-UT channel surrounding with presentation of key interacting residues. The urea transport channel of zf-UT is depicted by white dotted line with the inner urea molecules displayed as stick-balls. The conserved Q<sup>Pb</sup>–T<sup>5b</sup>–T<sup>5a</sup>–Q<sup>Pa</sup> motif is shown as green dots. **g, h** The interactions between urea and the key residues in the zf-UT urea transport channel (shown as blue dots) in the extracellular side (**g**) and the intracellular side (**h**) of the channel. The H-bonds are shown as red dashed line. **i** Barcode comparisons of the residues involving in the urea channel of zf-UT between different UTs. The residues predicted to involve with common interactions with urea molecules are displayed as black circles, including residues of the Q<sup>Pb</sup>–T<sup>5b</sup>–T<sup>5a</sup>–Q<sup>Pa</sup> motif filled with green, while the residues predicted to form distinct interactions are shown as black circles filled with gray. The letters inside the circles represent different amino acids present in the corresponding positions.

### Structural basis of uncompetitive inhibition of UT-A by CF11

In contrast to the competitive inhibition mode of 25a and ATB3, UTA<sub>inh</sub>-F11(CF11) was reported as an uncompetitive inhibitor of UT-A, with an EC<sub>50</sub> approximately 10 times better for UT-A1 than UT-B (Supplementary Table 4). The IC<sub>50</sub> of CF11 toward hUT-A2 was determined to be 2.78 ± 0.32 μM (Fig. 8a and Supplementary Table 4). Importantly, CF11 was observed only on the intracellular side of hUT-A2, without detectable EM density on the extracellular side (Fig. 8b–d and Supplementary Fig. 10e, f). These observations suggested that urea can still bind to the extracellular side of UT-A2 but cannot be transported into the intracellular side; thus, the interaction is unproductive (bound but not released). We therefore speculated that the specific binding mode of CF11 provides a mechanistic explanation for the uncompetitive inhibition of CF11 (Fig. 8b).

On the intracellular side, CF11 is located in the cavity surrounded by helices 3a–4a, Pa, ICL2a, and LICL (Fig. 8c). CF11 is a γ-sultambenzosulfonamide-type inhibitor, with two benzene rings connected by a nitrogen-sulfur bond. The methoxy group of CF11 inserts into CUBP but does not contact T176, V68, and F341 and only forms hydrophobic contacts with Q67<sup>Pa</sup> and F70<sup>Pa</sup>, leaving an empty space in the UT transport channel (Fig. 8d, e and Supplementary Table 7). Therefore, CF11 cannot compete with urea molecules to form polar interactions with the Q231<sup>Pb</sup>–T338<sup>5b</sup>–T176<sup>5a</sup>–Q67<sup>Pa</sup> motif of the CUBP, a common feature shared by competitive inhibitors 25a and ATB3. These structural features provided additional insights into the uncompetitive inhibition mode of CF11.

The specific residues encompassing the uncompetitive inhibitor CF11 were named the uncompetitive binding pocket (UCBP) (Fig. 8e). Inside the UCBP, CF11 formed hydrophobic interactions with A115<sup>3a</sup>, M299<sup>3b</sup>, L363<sup>ICL</sup>, and V366<sup>LICL</sup>. The two benzene rings of CF11 form π–π stacking interactions with F120<sup>3a</sup>, whereas the nitrogen-sulfur atoms connecting the two benzene rings form hydrogen bonds with the hydroxyl group of Y123<sup>3a</sup> and the main chain atoms of V174<sup>5a</sup>–F175<sup>5a</sup>. In addition, CF11 participates in π–π stacking with F300<sup>3b</sup> (Fig. 8d, e). According to the sequence alignment of different UTs, we found that two nonconserved amino acids in UCBP, A115<sup>3a</sup> and F120<sup>3a</sup> of hUT-A2, may contribute to the selectivity of F11 (Fig. 8f–h). Notably, A115<sup>3a</sup> in UT-A2 is replaced by L116<sup>3a</sup> in UT-B, which may provide steric hindrance to the chlorine atom of CF11, decreasing the binding affinity (Fig. 8f, g). This speculation was supported by structure-function relationship studies: replacing the chlorine atom with a hydrogen atom in CF11 improved the inhibition potency against UT-B<sup>20</sup>. Moreover, F120<sup>3a</sup> of hUT-A2 is replaced by L in hUT-A3 and hUT-B, losing π–π stacking with the benzene rings of CF11 (Fig. 8f, g). Therefore, A115<sup>3a</sup> and F120<sup>3a</sup> of UCBP are key residues of hUT-A2 that contribute to the selectivity of CF11, and we named the pocket the “A-F UCBP”. In summary, specific UCBP residues of UT-A2, such as A115<sup>3a</sup> and F120<sup>3a</sup>, could be utilized for inhibitor design targeting hUT-A2 for both uncompetitive inhibition and selectivity (Fig. 8i).

### Mechanism of noncompetitive inhibition of UT-A by targeting an “SCG” pocket

The 8-hydroxyquinoline derivative UTA<sub>inh</sub>-A2 (HQA2) is a non-competitive inhibitor of UT-A, with selectivity against UT-B of more than tenfold (IC<sub>50</sub> for UT-A1 vs. UT-B is approximately 5 μM vs. 50 μM) (Supplementary Table 4)<sup>21</sup>. The IC<sub>50</sub> values of HQA2 for blocking urea transport mediated by hUT-A2 were 3.66 ± 0.09 μM (Fig. 9a). In the HQA2-hUT-A2 complex structure, only one binding site located on the extracellular side of hUT-A2, located in the cavity surrounded by helices 3a, 3b–4b, and Pb, and the LECL, and ECL2b (Fig. 9b, c). Distinct from all other competitive inhibitors and uncompetitive inhibitors, which bind perpendicularly to the extracellular side of UT, HQA2 binds parallel to hUT-A2. Notably, the benzene ring of HQA2 is located in EBBP1 and EBBP2 (EBBP1-2). In EBBP1-2, the benzene ring of HQA2 forms π–π stacking with F135<sup>3c</sup> and hydrophobic interactions with L202<sup>ECL</sup>, L284<sup>3b</sup>, P335<sup>ECL2b</sup>, and P336<sup>ECL2b</sup>, including interactions with the “L-P” selective pocket (Fig. 9d, e and Supplementary Table 8). In particular, the methoxy group in the benzene ring of HQA2 extends into the EUBP, forming a hydrogen bond with the side chain of Q231<sup>5b</sup> (Fig. 9d, e), without occupying the entire EUBP or the CUBP, thereby affording a potential mechanism of noncompetitive inhibition of urea transport.

Importantly, the hydroxyquinoline moiety is rotated by approximately 90° and occupies a side pocket encompassing 6 residues with small side chains, named the SCG pocket (Supplementary Fig. 10g). In the SCG pocket, the hydroxyl group of the hydroxyquinoline moiety forms a hydrogen bond with the side chain of S279<sup>3b</sup> and van der Waals interactions with T275<sup>ECL1b</sup>, C285<sup>3b</sup>, G322<sup>4b</sup>, and A323<sup>4b</sup> (Fig. 9d and Supplementary Fig. 10h, i). Sequence alignment showed that the amino acid sequences in the SCG pockets of different UTs are not conserved, especially for residues S279<sup>3b</sup>, C285<sup>3b</sup>, and G322<sup>4b</sup> (Figs. 7i, 9f). Importantly, mutations of SCG pocket residues to structural equivalent residues in other UT members, such as S279D or C285W, significantly decreased the activity of HQA2 in blocking urea transportation (Fig. 9a and Supplementary Fig. 7k, l). These results suggested that this pocket has potential for designing hUT-A/B selective inhibitors. Moreover, the region where the SCG pocket is located is completely independent of the urea transport channel of hUT-A2 and may therefore serve as an allosteric pocket for ligand binding to regulate UT-mediated urea transportation (Fig. 9e–g).

### Discussion

In the present study, we determined 11 cryo-EM structures of four UT members, including hUT-A2, hUT-A3, hUT-B and zf-UT, in resting states (apo structure) and bound with urea, two synthetic competitive inhibitors, one uncompetitive inhibitor and one noncompetitive inhibitor. These structures not only provided direct snapshots for the observation of urea transport through UTs but also revealed the structural mechanisms underlying urea transport and selective inhibitor design targeting UT-A2 in competitive, uncompetitive and non-competitive modes, offering the potential to create a new class of

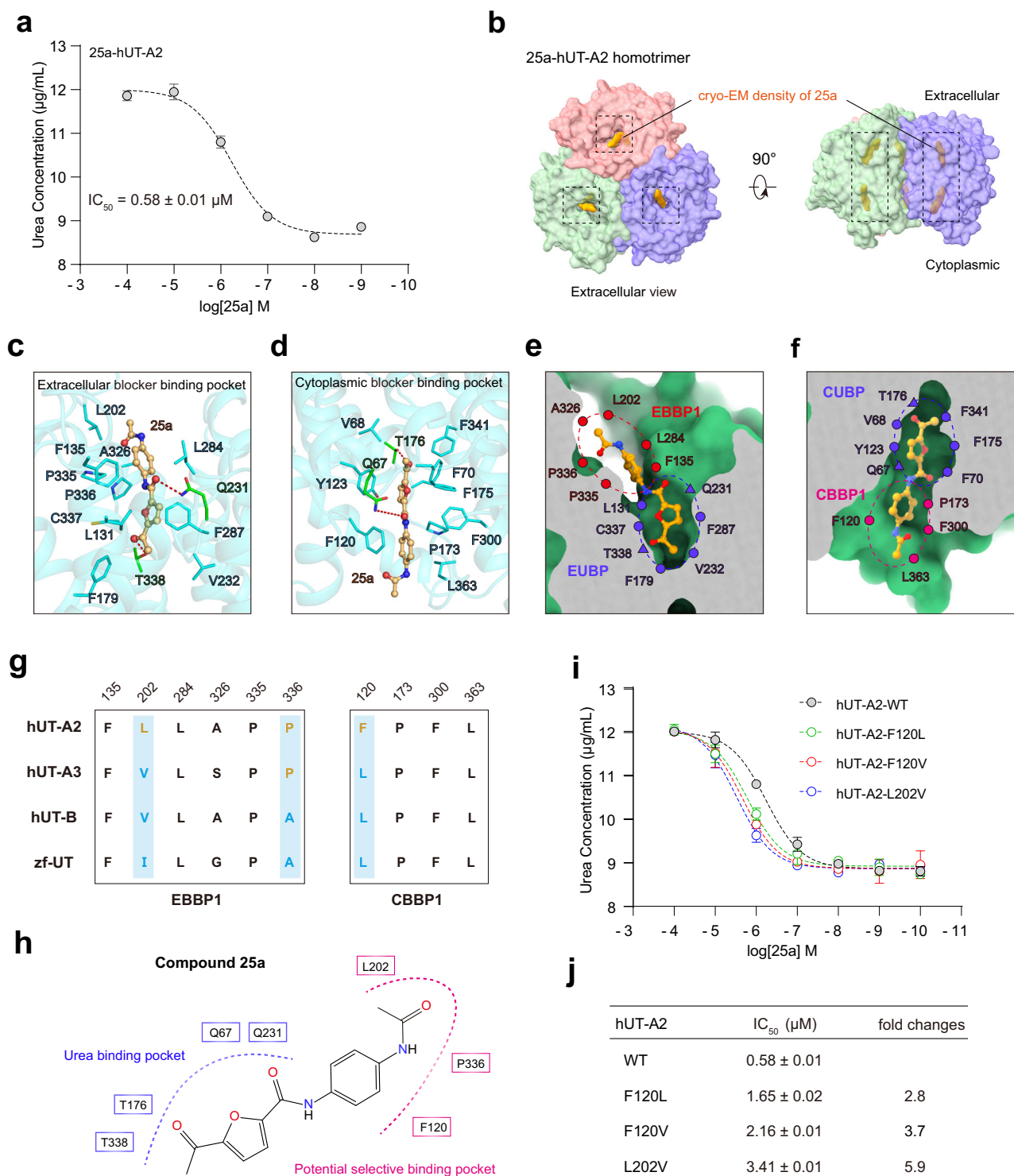
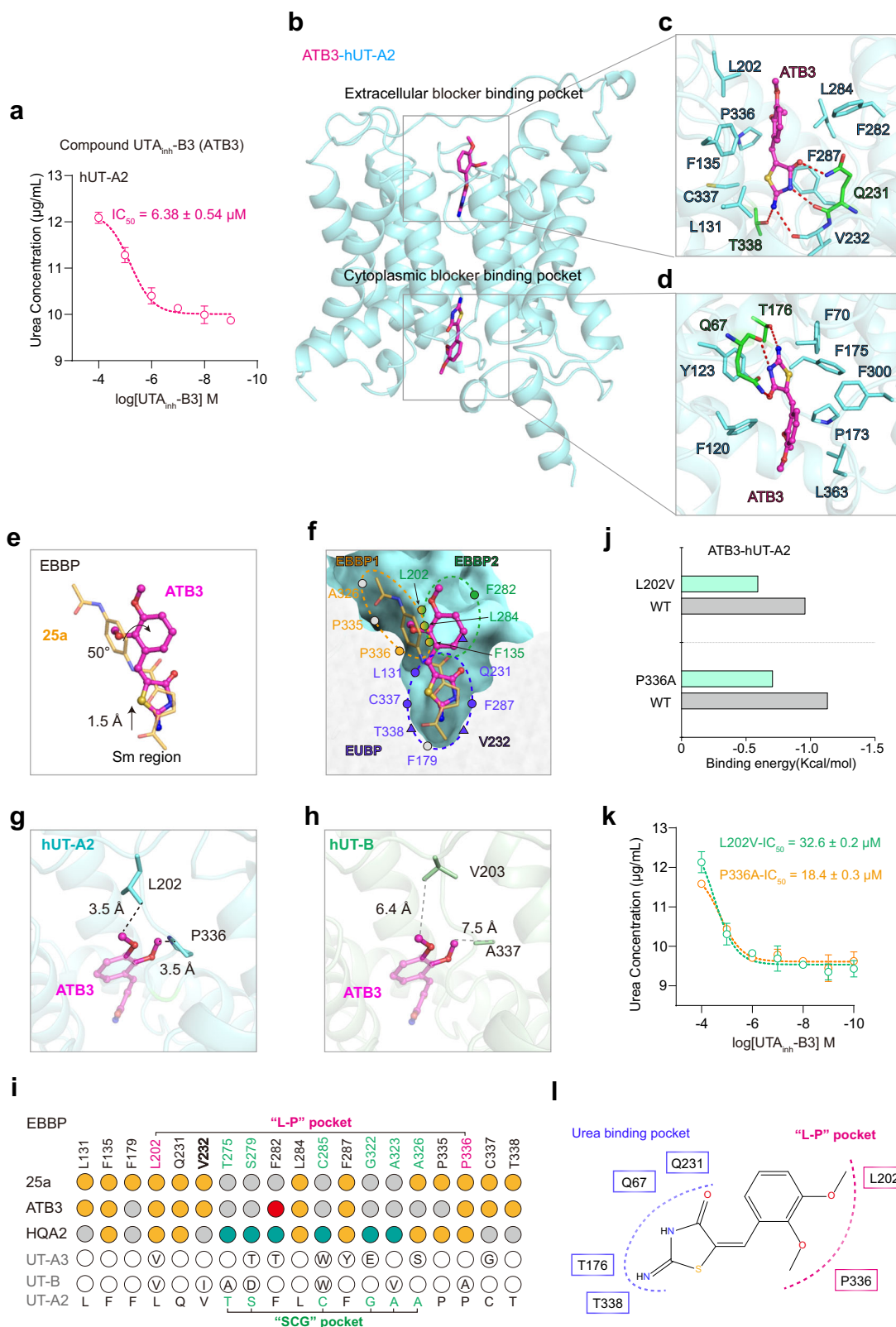


**Fig. 6 | The mechanism of inhibition of hUT-A2 by 25a.** **a** The concentration dependent blockade of urea transport of hUT-A2 by 25a using urease assay. Data are shown as mean  $\pm$  SEM of three independent experiments ( $n = 3$ ). **b** The cryo-EM density (orange) of 25a in hUT-A2 homotrimer from top view or side view. The surfaces of three hUT-A2 monomer are represented by orange, green and blue, respectively. **c, d** The interactions between hUT-A2 and 25a in extracellular blocker binding pocket (EBBP) (**c**) or cytoplasmic blocker binding pocket (CBBP) (**d**). The hUT-A2 are represented in blue cartoon and the key amino acids are represented by blue sticks. The 25a was represented by orange stick-ball. **e, f** The cutaway view of binding pockets of 25a in extracellular side (**e**) or cytoplasmic side (**f**). In the extracellular side, the 25a occupied two subpockets, the EBBP1 (extracellular blocker binding pocket 1) and EUBP (extracellular urea binding pocket), represented by red or blue dashed line respectively. In the intracellular side, the 25a

occupied CBBP1 (violet) and CUBP (blue). Residues forming polar interactions or hydrogen bonds with 25a are depicted using triangles. Residues only forming hydrophobic or van der Waals interactions are depicted as solid round circles. The 25a are represented by stick-ball and the hUT-A2 is represented by surface. **g** Sequence alignment of different UTs in the EBBP1 and CBBP1 regions. The non-conserved amino acids are highlighted with blue background. **h** The diagram of 25a engaging with the urea binding pocket or potential selective binding pocket with the interfaces represented by blue or violet dashed lines, respectively. Key residues interacting with 25a in these two pockets are shown in blue and violet rectangles, respectively. **i, j** Effects of hUT-A2 mutants F120L, F120V and L202V on the 25a activity toward hUT-A2 using urease assay. Values are mean  $\pm$  SEM from three independent experiments ( $n = 3$ ). The fold changes of  $\text{IC}_{50}$  are calculated by dividing the mean value of the mutants by the mean value of the wild type.



diuretics. Notably, compared with the apo-hUT-A2 structure, the binding of urea induced inward movements of residues along the urea transport channel in the urea-hUT-A2 complex structure, leading to a shrinkage of the channel radius by approximately 0.3 Å. Further structural analysis, combined with MD simulation, sequence alignment and mutational analysis, indicated that the urea recognition motif (URM), which comprises Q67<sup>Pa</sup>V68<sup>Pa</sup>Y123<sup>3a</sup>T176<sup>5a</sup> in the CUBP and

Q231<sup>Pb</sup>V1232<sup>Pb</sup>F/Y287<sup>3b</sup>T338<sup>5b</sup> in the EUBP, is conserved among most UT members and is responsible for urea recognition and transportation. In particular, rotating urea via H-bond transfer through the Q231<sup>Pb</sup>-T338<sup>5b</sup>-T176<sup>5a</sup>-Q67<sup>Pa</sup> polar motif along the transport channel may be the key to the driving force for urea transport. We have also conducted MD simulations of the process of urea permeation based on the urea-bound hUT-A2 and zf-UT structures. It is worth to note that



**Fig. 7 | The mechanism of inhibition and selectivity of Compound ATB3 toward hUT-A2.** **a** The concentration dependent blockade of urea transport of hUT-A2 by compound ATB3. Data are shown as mean  $\pm$  SEM of three independent experiments ( $n = 3$ ). **b** The extracellular blocker binding pocket (EBBP) and cytoplasmic blocker binding pocket (CBBP) of ATB3 in hUT-A2. **c, d** The interactions between hUT-A2 and ATB3 in EBBP (**c**) or CBBP (**d**). The H-bonds are shown as red dashed lines. **e** Structural comparison of 25a and ATB3 in EBBP. **f** The ATB3 occupied three subpockets in the extracellular side, the EBBP1, EBBP2, and EUBP. Residues forming polar interactions or hydrogen bonds with ATB3 are depicted using triangles. Residues forming hydrophobic or van der Waals interactions are depicted as solid round circles. The residues F135, L202, and L284 are shared by both EBBP1 and EBBP2. **g, h.** The methoxy groups of ATB3 formed hydrophobic interaction with L202 and P336 in hUT-A2, whereas ATB3 don't form similar interactions with structural equivalent amino acid V203 and A337 in hUT-B. The

black dashed lines represent the shortest distance. **i** Barcode comparisons of the residues involving in the EBBP of different UTs. The residues engaged interactions with 25a, ATB3 and HQA2 are colored orange, and the special residues only interact with ATB3 or HQA2 are colored red or green, respectively. The amino acid of hUT-A2 are displayed on the top line and bottom, with the residues in "L-P" pocket and "SCG" pocket colored magenta and green, respectively. The letters inside the black circles represent the non-conserved amino acids of hUT-A3 or hUT-B. **j** The comparison between the best estimate residue energy contributions of residues L202 or P336 for their interaction with ATB3 and their corresponding L202V, P336A mutants. **k** Effects of hUT-A2 mutants L202V and P336A on the ATB3 activity toward hUT-A2. Values are mean  $\pm$  SEM from three independent experiments ( $n = 3$ ). **l** The diagram of ATB3 engaging with the urea binding pocket or "L-P" pocket with the interfaces represented by blue or violet dashed lines, respectively.

the calculation of the free energy changes in urea molecules passing through the transport channel is still challenging and variable, because urea needs to get rid of water to pass Sm region and the role of waters in the urea permeation process is not yet clear<sup>22–24</sup>. Our results showed that significant energy barriers are found in the Sm region compared to the Si and So regions, and the valley values of the free energy in the Sm region are higher than those in the Si and So regions. These features of the energy are consistent with the structural information of the urea-bound UTs and the MD simulation of urea permeation processes described by Ming Han et al.<sup>19,22,25</sup> (Supplementary Table 9). Combining the MD simulation results with the information offered by structural models and biochemical experiments, we finally speculated that the urea transport route is as follows (Supplementary Movie): (1) the extracellular free urea molecule is first captured by H-bonding to the side chain of Q231<sup>Pb</sup> and then enters the So region. The binding of urea within the EUBP is further stabilized by the formation of another hydrogen bond with T338<sup>Sb</sup>. (2) The urea molecule is guided into the Sm region of the channel by a swing of the T338<sup>Sb</sup> side chain. In the Sm region, urea molecules alternately form hydrogen bonds with the side chains of T338<sup>Sb</sup> and T176<sup>Sa</sup>, reorienting the oxygen atom of urea. (3) A swing of the T176<sup>Sa</sup> side chain rotates the urea molecule for transfer to the Si region in the CUBP. (4) With the movement of the Q67<sup>Pa</sup> side chain in the CUBP, urea molecules leave the Si region and enter the cell, completing transport. In addition, the movement of urea molecules in the channel is restricted by the hydrophobic amino acid pairs on both sides of the channel, so that only one urea molecule at one time is allowed to pass through a given position in the channel, and this mechanism ensures that urea molecules are transported across the membrane in only one direction at a time. Notably, we didn't include water in our simulation, which needs further exploration. A similar mechanism is proposed for zf-UT according to structural observation, MD simulation and mutational analysis.

Selective inhibitors of UT are a potential new class of salt-sparing diuretics. Notably, structural analysis revealed that the competitive, uncompetitive and noncompetitive inhibitors bind to hUT-A2 via distinct modes and different binding pockets. Two competitive inhibitors, 25a and ATB3, occupy both the EUBP and the CUBP, competing with urea for H-bonding with the "Q<sup>Pb</sup>-T<sup>Sb</sup>-T<sup>Sa</sup>-Q<sup>Pa</sup>" motif, thus providing a mechanism of competitive inhibition. Moreover, the non-conserved residues L202<sup>ECL</sup> and P336<sup>ECL2b</sup> in the EBBP of hUT-A2 (also called the LP pocket) interact with both competitive inhibitors and could be utilized for the design of selective competitive inhibitors of hUT-A2. Distinct from competitive inhibitors, the uncompetitive inhibitor CF11 and noncompetitive inhibitor HQA2 bind to hUT-A2 in two different pockets localized on either the cytoplasmic or extracellular side, named the UCBP and the SCG, respectively. Whereas the binding of CF11 solely at the cytoplasmic side via the UCBP allow urea entry but blocks urea transport, the SCG pocket may be utilized as an allosteric site for inhibitor design. In addition, key residues in the UCBP and SCG pocket were identified for selective inhibitor design targeting hUT-A2,

which is half part of hUT-A1 C-terminal. Moreover, our structures reveal that certain UT inhibitors, such as CF11, exclusively bind to the intracellular pocket of the urea transporter. These inhibitors require membrane crossing to exert their inhibitory effect (Supplementary Table 10) on urea transport, suggesting that it is crucial to take into account the transmembrane efficiency for modifying the UTA<sub>inh</sub>-F type urea channel blockers as intracellular binders. Taken together, our study not only afforded direct observation and a structural understanding of urea transport via UTs but also provided a landscape of the structural basis of hUT-A2 inhibition by different inhibitors, which may facilitate the design of selective hUT-A inhibitors with either competitive, uncompetitive or noncompetitive modes.

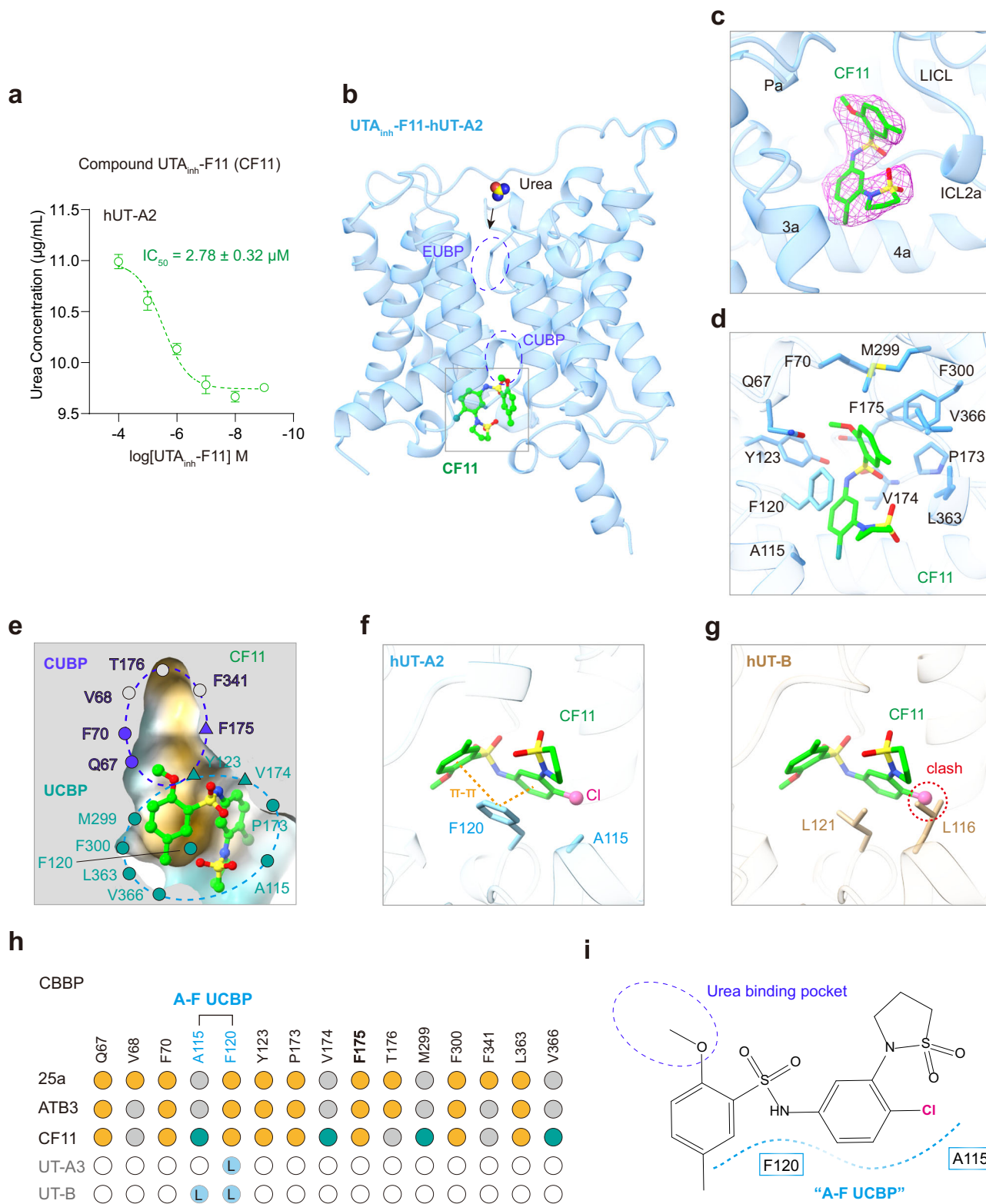
## Methods

### Constructs

The human UT-A1, -A2, -A3, -B and zebrafish UT genes were cloned into pcDNA3.1 and pFastBac1 vector for functional assays and protein expression, respectively. To facilitate expression and purification, the full-length sequence of these UTs were introduced into the pcDNA3.1 or pFastBac1 expression vector with a Flag tag at the N terminus, and a Tobacco Etch cleavage site and mCherry sequence were added to the C-terminus.

### Measurement of receptor cell-surface expression by western blot

To accomplish comparative plasma membrane expression levels of wild type and mutants of hUT-A2, hUT-A3, hUT-B and zf-UT, the plasmid amount were adjusted and transfected into HEK293 cells, and their expression levels were confirmed by Western blot. HEK293 cells were transiently transfected with pcDNA3.1-hUT-A2, pcDNA3.1-hUT-A3, pcDNA3.1-hUT-B, pcDNA3.1-zf-UT, hUT-A2 mutants or zf-UT mutants, respectively. Forty-eight hours after transfection, the transfected HEK293 cells were collected and then washed in pre-colded HBSS buffer and centrifuged at 600 g at 4 °C for 5 min. And then the cell pellets were homogenized and centrifugated at 600 g at 4 °C for 30 min to remove fractions of nuclei and cell apparatus. The supernatant was further centrifugated at 60,000 g at 4 °C for 30 min to collect the cell membranes. The membranes were then homogenized and solubilized with HBSS buffer containing 1% (w/v) DDM and protease inhibitor for 2 h at 4 °C with end-to-end rotation. After that, the solubilized membrane supernatant was collected by centrifugated at 60,000 g for 30 min to remove the precipitate, and then were subjected to SDS-polyacrylamide gel electrophoresis and Western blot for further analysis. For detection of the hUT-A2, hUT-A3, hUT-B, zf-UT, the anti-FLAG (1:1000, Sigma, F1804) primary antibody and HRP-conjugated goat anti-mouse IgG (1:5000, ThermoFisher, A16066) secondary antibody were used. For detection of the membrane reference, the anti-ATPIA1 (1:1000, Proteintech, 14418-1-AP) primary antibody and the HRP-conjugated goat anti-rabbit IgG (1:5000, Sigma Aldrich, A6154) secondary antibody were used.



### Detection of urea transportation by using <sup>14</sup>C-labeled urea

HEK293 cells were transfected with different UTs or their mutants by using Polyethyleneimine (PEI) with a volume ratio at 1:3 of plasmids and PEI. After transfection for 48 h, each well was incubated with 300 μl of DMEM supplemented with 10 mmol/L urea and 1 μCi of <sup>14</sup>C-urea for 30 min. After incubation, the cells were rinsed three times with cold 1 × PBS for 20 s each time. Subsequently, 500 μl of 10% SDS

was added to each well to lyse the cells for 5 min. The resulting cell lysate was then combined with 5 ml of scintillation fluid in a scintillation vial for subsequent measurement using a scintillation counter. In the experiment evaluating the inhibitory function of the inhibitor, 100 μmol/L of 25a was added to DMEM with 10 mmol/L urea and 1 μCi of <sup>14</sup>C-urea in or the 1 × PBS buffer for incubation or washing. And the remaining steps remained unchanged.

**Fig. 8 | The structural characterization of Compound UTA<sub>inh</sub>-F11 binding to hUT-A2.** **a** The concentration dependent blockade of urea transport of hUT-A2 by Compound UTA<sub>inh</sub>-F11 (CF11). Data are shown as mean  $\pm$  SEM of three independent experiments ( $n = 3$ ). **b** The CF11 bound in the cytoplasmic side of hUT-A2 without occupying the urea binding pocket. **c** The cryo-EM density of CF11 (red mesh) contoured at 4.0  $\sigma$  level is located in a cavity surrounded by helices 3a–4a, Pa, ICL2a, and L1CL. **d** The key residues of hUT-A2 in CF11 binding pocket are shown by blue sticks. The CF11 is represented by green stick-ball. **e** The cutaway view of the binding pocket of CF11. The EUBP and the CUPB are represented by blue and green dashed line, respectively. Residues forming polar interactions or hydrogen bonds with CF11 are depicted using triangles. Residues only forming hydrophobic or van der Waals interactions are depicted as solid round circles. **f, g** Comparison of different amino acids in the CF11 binding pocket between hUT-A2 (**f**) and hUT-B (**g**).

The A115<sup>3a</sup> of hUT-A2 is replaced by L116<sup>3a</sup> of hUT-B, thus cause a steric hindrance to the chlorine atom of CF11. The F120<sup>3a</sup> of hUT-A2 is replaced by L in hUT-B, therefore losing  $\pi$ - $\pi$  stacking (orange dashed lines) with the benzene rings of CF11. **h** Barcode comparisons of the residues involving in the CBBP of different UTs. The residues participated in interactions with 25a, ATB3, and CF11 are displayed as black circles filled orange, and the special residues only interacting with CF11 are shown as black circles filled green. The amino acid sequences of hUT-A2 are shown on top, with the special residues involving in “A-F UCBP” marked by light blue color. The letters inside the black circles filled with light blue represent the non-conserved amino acids in the “A-F UCBP” of hUT-A3 or hUT-B. **i** The diagram of binding mode of CF11, with the hUT-A2 interfaces represented by blue or light blue dashed lines, respectively. Key residues interacting with CF11 in “A-F UCBP” are shown in blue and light blue rectangles, respectively.

### Detection of urea transportation and the effect of inhibitors by using the urease assay

HEK293 cells were transfected with different UTs or their mutants using Polyethyleneimine (PEI). After transfection for 48 h, the cells were resuspended and divided into aliquots. The aliquots were incubated with 50  $\mu$ M/L urea and different concentrations of each inhibitor, and then reach equilibrium state by shaking at 200 rpm in 37 °C incubators. After equilibrium, cells were collected by centrifuged at 200 g and washed with HBSS buffer containing corresponding concentration inhibitor for 1 min. After washing, cells were diluted in water, and broken by 300 W ultrasonication for 3 min to release the reserved urea. To detect the urea amount, we followed the instruction of the BUN detection kit (BC1535, Solar-bio Life Sciences, Beijing,). Firstly, the broken cells were centrifuged at 25,000 g for 15 min, and the supernatant were mixed with reagent I and reagent II and incubated at 37 °C for 10 min. After incubation, they were mixed with reagent III and reagent IV and incubated at 37 °C for 30 min. Finally, the enzyme catalyzed solutions were measured with microplate-reader under 630 nm wavelength. The urea concentrations were calculated by compared to the standard urea solution. And the inhibition effects were represented by dose curve fitted by three-parameter dose-response model using GraphPad software.

### Expression and purification of different UT proteins in SF9 cells

Recombinant baculovirus was generated using the Bac-to-Bac Baculovirus Expression System (Invitrogen). Briefly, FuGENE HD transfection reagent (Promega) was used to prepare baculovirus. SF9 insect cells were seeded in ESF921 medium at a density of  $2.5 \times 10^6$  cells/ml and infected with zf-UT, hUT-A2, hUT-A3 or hUT-B baculovirus. After 48 h incubation at 27 °C, shaking at 110 rpm, cells were collected by centrifugation, flash-frozen in liquid nitrogen and stored at -80 °C. For structural determination, the cells were resuspended in lysis buffer (20 mM HEPES, pH 7.4, 100 mM NaCl, 5 mM CaCl<sub>2</sub>, 2.5 mg/ml leupeptin and 0.2 mg/ml benzamidine) and grinded into membranes with Dounce. The cell lysate was then solubilized by 0.5% (w/v) lauryl maltose neopentylglycol (LMNG; Anatrace) and 0.1% (w/v) cholesteryl hemisuccinate TRIS salt (CHS; Anatrace) for 2 h at 4 °C. The supernatant was collected by centrifugation at 25,000 g for 30 min, and the solubilized sample solution was incubated with M1 anti-FLAG resin for 2.5 h at 4 °C. The sample solution was immobilized on Flag-M1 resin, loaded on a Flag-M1 column, and washed with 20 column volumes of 20 mM HEPES, pH 7.4, 100 mM NaCl, 5 mM CaCl<sub>2</sub>, 0.01% (w/v) LMNG, 0.002% (w/v) CHS, 2.5 mg/ml leupeptin and 0.2 mg/ml benzamidine. The protein solution was then eluted with 20 mM HEPES, pH 7.4, 100 mM NaCl, 2.5 mg/ml leupeptin, 0.2 mg/ml benzamidine, 0.0005% (w/v) LMNG, 0.0001% (w/v) CHS, 10 mM EDTA and 0.2 mg/ml FLAG peptide (GL Biochem). The protein solution was collected and concentrated, then loaded onto a Superose 6 Increase 10/300 GL column (Cytiva) with buffer containing 20 mM HEPES, pH 7.4, 100 mM NaCl, 0.00075% (w/v) LMNG, 0.0002% (w/v) CHS. The protein fractions were concentrated with a 100 kDa MWCO Millipore concentrator. In order to prepare the complex of

inhibitor and UT, 10  $\mu$ M to 100  $\mu$ M of inhibitors 25a, ATB3, CF11, and HQA2 were separately added to the above concentrated sample solution and incubated on ice for at least half an hour.

### Glutaraldehyde crosslinking

In order to mildly crosslink the UT trimer, an ‘on-column’ crosslinking method was used<sup>26</sup>. First, 200  $\mu$ l, 0.25% glutaraldehyde was injected to a pre-equilibrated Superose 6 Increase 10/300 GL column (in 20 mM HEPES, pH 7.4, 100 mM NaCl, 0.00075% (w/v) LMNG, 0.0002% (w/v) CHS) and run at 0.25 ml/min for 20 min. Subsequently, the column flow was paused, and the injection loop was flushed using buffer followed by injection of purified UT solution. Subsequently, the column was run at 0.25 ml/min and 0.3 ml fractions were collected.

### Cryo-grid preparation and EM data collection

For cryo-EM grid preparation, the purified UTs after crosslinking homotrimer protein were concentrated to a concentration of 2 mg/ml and applied as 3  $\mu$ l aliquots onto glow-discharged holey carbon grids. Grids were transferred to a Titan Krios electron microscope (300 kV) equipped with spherical aberration (Cs) image corrector. Images were acquired with a Gatan K3 Summit or Falcon counting camera at a nominal magnification of  $\times 130,000$ , with pixel sizes on the object scale ranging from 0.82 Å to 1.055 Å, respectively. The Thermo Scientific EPU equipped with customized scripts enabled the automated low-dose image acquisition and the movie stacks were obtained with a defocus range of -1.0 to -2.0  $\mu$ m. The accumulated dose was set to 60 electrons per Å<sup>2</sup> and a total of 32 frames per micrograph.

### Image processing and 3D reconstructions

The overall cryo-EM data processing pipeline for all UTs structures are shown in Supplementary Figs. 2–4. Initial Cryo-EM movie stacks were summed and subjected to Patch Motion Correction dose-weighting and patch CTF estimation in CryoSPARC<sup>27</sup> depending on its image processing software.

For apo-hUT-A2 structures, 8034 movie stacks were imported in cryoSPARC v4.2. Each micrograph was manually inspected to take away bad pictures that were contaminated by crystalline ice or other visible contamination. For purpose of better particle-picking, a conventional neural network-based method Topaz implemented in CryoSPARC<sup>28</sup> was used for particle picking. Total 2,530,038 particles were extracted with 288 pixels from the dataset and subjected to 2D classification. A clean particle stack of 408,332 from the 2D classification step was selected and re-extracted with a box size of 288 pixels. This clean particle stack was subjected to ab-initio reconstruction and heterogeneous refinement with C3 symmetry served as 3D Classification. Then 183,080 particle projections of the best class were further applied for homogenous refinement and non-uniform refinement with C3 symmetry, generating the best density map with global resolution of 2.8 Å. The calculation processes for other UTs structures are the same as that for the apo-hUT-A2 structure. The detailed processes are shown in Supplementary Figs. 2–5.



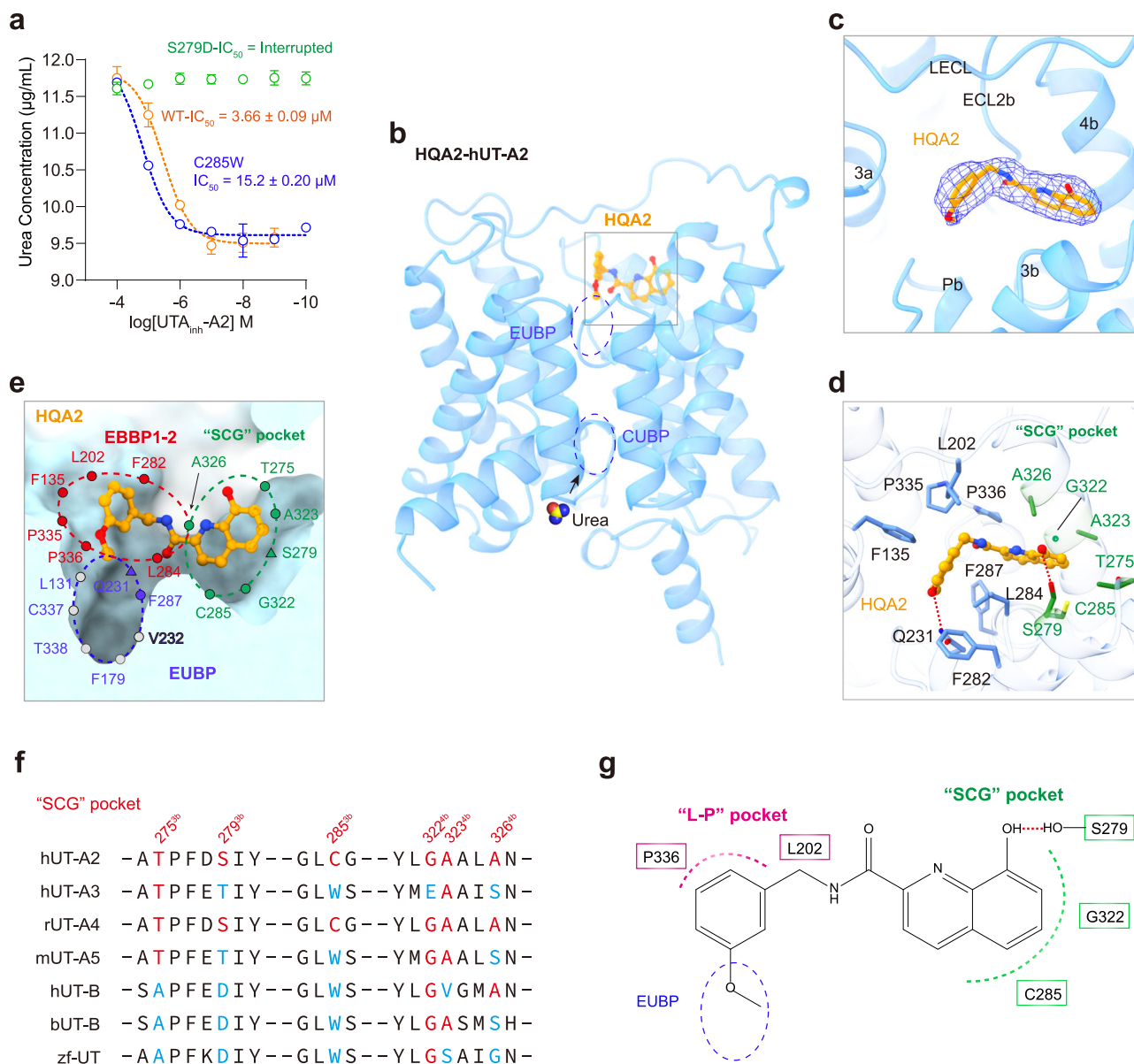


**Fig. 9 | Mechanism of noncompetitive blocking hUT-A2 by HQA2.** **a** The concentration dependent blockade of urea transport of wild type hUT-A2 and S279D, C285W mutants by HQA2. Values are mean  $\pm$  SEM from three independent experiments ( $n = 3$ ). **b** The HQA2 bound in the extracellular side of hUT-A2 without occupying the urea binding pocket. The hUT-A2 are represented in blue cartoon and the HQA2 shows as orange stick-ball. **c** The cryo-EM density (blue mesh) of HQA2 at the 4.0  $\sigma$  contour level is located in the cavity surrounded by helices 3a, 3b–4b, and Pb, and the LECL, and ECL2b. **d** The key residues of the HQA2 binding pocket of hUT-A2 are represented by sticks and the residues involving in the "SCG" pocket are colored green. The H-bond are shown as red dashed line. **e** The cutaway view of the binding pocket of HQA2 (orange stick-ball). The EUBP, EBBP1-2 and the noncompetitive "SCG" pocket are represented by blue, red and green dashed line respectively. Residues forming polar interactions or hydrogen bonds with HQA2 are depicted using triangles.

### Model building and structure refinement<sup>29–32</sup>

The initial template of all the UT structures were derived from the *Desulfovibrio Vulgaris* UT structure (PDB: 3K3F) using Phyre online server, respectively. Models were rigidly docked into the cryo-EM density map and saved as new models with the coordinates relative to cryo-EM map using UCSF Chimera. All separated coordinates were merged into one PDB file by manual building and adjustment in COOT. The final model was subjected to global refinement and minimization in real space using PHENIX for cryo-EM maps. The

Residues only forming hydrophobic or van der Waals interactions are depicted as solid round circles. The HQA2 are represented by orange stick-ball and the hUT-A2 are represented by surface. **f** Sequence alignment of the structurally equivalent residues in the noncompetitive SCG pocket of hUT-A2 compared with other UT members including hUT-A3, rUT-A4 (rat UT-A4), mUT-A5 (mouse UT-A5), hUT-B, bUT-B (bovine UT-B) and zf-UT. Key residues of SCG pocket in hUT-A2 are shown in red font on the top line. Sequences with the same amino acids as the SCG pocket of hUT-A2 are represented in red, while those with non-conserved amino acids are represented in light blue. **g** The diagram of HQA2 engaging with the extracellular urea binding pocket (EUBP), L-P pocket and the noncompetitive SCG pocket with the interfaces represented by blue, violet and green dashed lines, respectively. Key residues interacting with L-P pocket and SCG pocket are shown in violet and green rectangles, respectively. The H-bond between HQA2 and residues S279 is shown as red dashed line.

Figures were prepared with Chimera and PyMOL (<http://pymol.org/>).

### Molecular dynamics simulations and binding energy calculation

To explore the binding energy of wild type and mutant ATB3 or 25a in hUT-A2, all-atom molecular dynamics simulations were conducted. The simulation model, derived from the cryo-EM structure of the trimer complex within this study, was employed. The CHARMM36m force field<sup>33</sup> was used for wild type and mutant hUT-A2-ATB3 or 25a-

hUT-A2, lipids, ions, and TIP3P water molecules, consistent with prior research. System setup involved CHARMM-GUI<sup>34</sup> for generating MD input files. The wild type and mutant ATB3-hUT-A2 or 25a-hUT-A2 complex was embedded in a pre-equilibrated 1-palmitoyl-2-oleoyl-sn-glycero-3-phosphatidylcholine membrane and solvated in a hexagonal TIP3P water box (size:  $\sim 70 \text{ \AA} \times 70 \text{ \AA} \times 80 \text{ \AA}$ ) with 0.15 M NaCl added for charge neutralization. Membrane orientation relied on the Orientations of Proteins in Membranes database. Simulations began with initial energy minimization (10,000 steps) via Gromacs 2019.6<sup>35</sup> using a combination of steepest descent (5000 steps) and conjugated gradient (5000 steps) methods. Subsequent stages included heating the system from 0 to 310 K in the NVT ensemble over 1000 ps and production simulations at 1 atm in the NPT ensemble for over 1000 ps with  $10.0 \text{ kcal mol}^{-1} \text{ \AA}^{-2}$  harmonic restraints. The MD production (1000 ns) utilized a 2 fs time step, employing Gromacs 2019.6. Analysis comprised using the particle mesh Ewald method with a 12 Å cutoff for electrostatic interactions. Hydrogen bond constraints utilized the SHAKE algorithm (2 fs integration time step). Post-simulation analyses were performed using Gromacs 2019.6 and VMD<sup>36</sup>. Binding energy calculations employed the g\_mmpbsa package and the MM-PBSA method<sup>37</sup>, encompassing potential energy in vacuum, polar solvation energy, and non-polar solvation energy computations. Parameters included a solvent probe radius of 0.14 nm, solvent dielectric constant of 80, and solute dielectric constant of 2. Python scripts facilitated MM-PBSA calculations (MmPbSaStat.py) and assessment of individual residue contributions interacting with ATB3 (MmPbSaDecomp.py).

### Metadynamics simulations

Metadynamics<sup>38</sup> simulations were employed to investigate urea crossing pathways within the hUT-A2 and zf-UT channels. Gromacs 2019.6 and plumed 2.7.1<sup>39</sup> were used for this enhanced sampling technique. Gaussian hills were added at 500-step intervals, biasing the potential energy landscape with an initial height of  $10 \text{ kJ mol}^{-1}$  and a width of  $1000 \text{ kJ mol}^{-1}$ , controlled by a bias factor of 15. Two collective variables (CV1 and CV2) guided the metadynamics simulation of urea crossing the hUT-A2, zf-UT pathway. CV1 represented the distance between urea and Q67 center of mass, crucial for urea's transit. CV2 measured the distance between specific residues (V232/V68 and T338/T176), these residues affect the channel of urea through hUT-A2, zf-UT.

### Reporting summary

Further information on research design is available in the Nature Portfolio Reporting Summary linked to this article.

### Data availability

All data produced or analyzed in this study are included in the main text or the supplementary materials. Data supporting the findings of this manuscript are available from the corresponding authors upon request. The cryo-EM density maps and atomic coordinates have been deposited at the Electron Microscopy Data Bank under accession codes EMD-38270 (apo-hUT-A2), EMD-38271 (urea-hUT-A2), EMD-38268 (25a-hUT-A2), EMD-38272 (ATB3-hUT-A2), EMD-38273 (CF11-hUT-A2), EMD-38274 (HQA2-hUT-A2), EMD-38275 (apo-hUT-A3), EMD-38276 (apo-hUT-B), EMD-38277 (apo-zf-UT), EMD-38278 (urea-zf-UT) and EMD-38279 (25a-zf-UT), and Protein Data Bank under accession codes 8XD9 (apo-hUT-A2), 8XDA (urea-hUT-A2), 8XD7 (25a-hUT-A2), 8XDB (ATB3-hUT-A2), 8XDC (CF11-hUT-A2), 8XDD (HQA2-hUT-A2), 8XDE (apo-hUT-A3), 8XDF (apo-hUT-B), 8XDG (apo-zf-UT), 8XDH (urea-zf-UT) and 8XDI (25a-zf-UT). Molecular Dynamics trajectories have been uploaded to the Figshare repository [[https://figshare.com/articles/dataset/UT-MD\\_files/27605577?file=50190870](https://figshare.com/articles/dataset/UT-MD_files/27605577?file=50190870)]. The source data underlying Figs. 1c, e, g, 3g, h, 4i, 6a, i, j, 7a, k; 8a, 9a and Supplementary Figs. 1f, 7, 9 are provided as a Source Data file. Source data are provided with this paper.

### References

- Levin, E. J., Quick, M. & Zhou, M. Crystal structure of a bacterial homologue of the kidney urea transporter. *Nature* **462**, 757–761 (2009).
- Sebbane, F. et al. The *Yersinia pseudotuberculosis* Yut protein, a new type of urea transporter homologous to eukaryotic channels and functionally interchangeable in vitro with the *Helicobacter pylori* Urel protein. *Mol. Microbiol.* **45**, 1165–1174 (2002).
- Weeks, D. L., Eskandari, S., Scott, D. R. & Sachs, G. A H<sup>+</sup>-gated urea channel: the link between *Helicobacter pylori* urease and gastric colonization. *Science* **287**, 482–485 (2000).
- Hediger, M. A. et al. Structure, regulation and physiological roles of urea transporters. *Kidney Int.* **49**, 1615–1623 (1996).
- Smith, C. P. Mammalian urea transporters. *Exp. Physiol.* **94**, 180–185 (2009).
- Bagnasco, S. M. Role and regulation of urea transporters. *Pflugers Arch.* **450**, 217–226 (2005).
- Regan, M. D. et al. Nitrogen recycling via gut symbionts increases in ground squirrels over the hibernation season. *Science* **375**, 460–463 (2022).
- Yang, B. Transport characteristics of urea transporter-B. *Subcell. Biochem.* **73**, 127–135 (2014).
- Shayakul, C., Cl  men  on, B. & Hediger, M. A. The urea transporter family (SLC14): physiological, pathological and structural aspects. *Mol. Aspects Med.* **34**, 313–322 (2013).
- Nandi, S. et al. Urea transporter and its specific and nonspecific inhibitors: state of the art and pharmacological perspective. *Eur. J. Pharmacol.* **911**, 174508 (2021).
- Esteva-Font, C., Anderson, M. O. & Verkman, A. S. Urea transporter proteins as targets for small-molecule diuretics. *Nat. Rev. Nephrol.* **11**, 113–123 (2015).
- Smith, C. P., Potter, E. A., Fenton, R. A. & Stewart, G. S. Characterization of a human colonic cDNA encoding a structurally novel urea transporter, hUT-A6. *Am. J. Physiol. Cell Physiol.* **287**, C1087–C1093 (2004).
- Duchesne, R. et al. UT-A urea transporter protein in heart: increased abundance during uremia, hypertension, and heart failure. *Circ. Res.* **89**, 139–145 (2001).
- Yu, L. et al. Physiological functions of urea transporter B. *Pflugers Arch.* **471**, 1359–1368 (2019).
- Klein, J. D., Blount, M. A. & Sands, J. M. Urea transport in the kidney. *Compr. Physiol.* **1**, 699–729 (2011).
- Handley, R. R. et al. Brain urea increase is an early Huntington's disease pathogenic event observed in a prodromal transgenic sheep model and HD cases. *Proc. Natl. Acad. Sci. USA* **114**, E11293–E11302 (2017).
- Verkman, A. S. et al. Small-molecule inhibitors of urea transporters. *Subcell. Biochem.* **73**, 165–177 (2014).
- Chi, G. et al. Structural characterization of human urea transporters UT-A and UT-B and their inhibition. *Sci. Adv.* **9**, eadg8229 (2023).
- Levin, E. J. et al. Structure and permeation mechanism of a mammalian urea transporter. *Proc. Natl. Acad. Sci. USA* **109**, 11194–11199 (2012).
- Esteva-Font, C. et al. Diuresis and reduced urinary osmolality in rats produced by small-molecule UT-A-selective urea transport inhibitors. *FASEB J.* **28**, 3878–3890 (2014).
- Esteva-Font, C., Phuan, P. W., Anderson, M. O. & Verkman, A. S. A small molecule screen identifies selective inhibitors of urea transporter UT-A. *Chem. Biol.* **20**, 1235–1244 (2013).
- Han, M. & Chen, L. Y. Molecular dynamics simulation of human urea transporter B. *Mol. Simul.* **47**, 1022–1028 (2021).
- Yang, B. & Verkman, A. S. Urea transporter UT3 functions as an efficient water channel. Direct evidence for a common water/urea pathway. *J. Biol. Chem.* **273**, 9369–9372 (1998).

24. Wang, Z. et al. Computation and simulation of the structural characteristics of the kidney urea transporter and behaviors of urea transport. *J. Phys. Chem. B* **119**, 5124–5131 (2015).
25. McNulty, R., Ulmschneider, J. P., Luecke, H. & Ulmschneider, M. B. Mechanisms of molecular transport through the urea channel of *Helicobacter pylori*. *Nat. Commun.* **4**, 2900 (2013).
26. Shukla, A. K. et al. Visualization of arrestin recruitment by a G-protein-coupled receptor. *Nature* **512**, 218–222 (2014).
27. Punjani, A., Rubinstein, J. L., Fleet, D. J. & Brubaker, M. A. cryoSPARC: algorithms for rapid unsupervised cryo-EM structure determination. *Nat. Methods* **14**, 290–296 (2017).
28. Bepler, T. et al. Positive-unlabeled convolutional neural networks for particle picking in cryo-electron micrographs. *Nat. Methods* **16**, 1153–1160 (2019).
29. Kelley, L. A., Mezulis, S., Yates, C. M., Wass, M. N. & Sternberg, M. J. The phyre2 web portal for protein modeling, prediction and analysis. *Nat. Protoc.* **10**, 845–858 (2015).
30. Pettersen, E. F. et al. UCSF chimera—a visualization system for exploratory research and analysis. *J. Comput. Chem.* **25**, 1605–1612 (2004).
31. Emsley, P. & Cowtan, K. Coot: model-building tools for molecular graphics. *Acta Crystallogr. D: Biol. Crystallogr.* **60**, 2126–2132 (2004).
32. Adams, P. D. et al. PHENIX: a comprehensive python-based system for macromolecular structure solution. *Acta Crystallogr. D: Biol. Crystallogr.* **66**, 213–221 (2010).
33. Huang, J. et al. CHARMM36m: an improved force field for folded and intrinsically disordered proteins. *Nat. Methods* **14**, 71–73 (2016).
34. Lee, J. et al. CHARMM-GUI input generator for NAMD, GROMACS, AMBER, openMM, and CHARMM/OpenMM simulations using the CHARMM36 additive force field. *J. Chem. Theory Comput.* **12**, 405–413 (2015).
35. Van Der Spoel, D. et al. GROMACS: fast, flexible, and free. *J. Comput. Chem.* **26**, 1701–1718 (2005).
36. Humphrey, W., Dalke, A. & Schulten, K. VMD: visual molecular dynamics. *J. Mol. Graph* **14**, 27–38 (1996). 33–38.
37. Kumari, R., Kumar, R. & Lynn, A. g\_mmpbsa—a GROMACS tool for high-throughput MM-PBSA calculations. *J. Chem. Inf. Model.* **54**, 1951–1962 (2014).
38. Laio, A. & Gervasio, F. L. Metadynamics: a method to simulate rare events and reconstruct the free energy in biophysics, chemistry and material science. *Rep. Prog. Phys.* **71**, 126601 (2008).
39. Tribello, G. A., Bonomi, M., Branduardi, D., Camilloni, C. & Bussi, G. PLUMED 2: new feathers for an old bird. *Comput. Phys. Commun.* **185**, 604–613 (2014).

## Acknowledgements

This work was supported by the National Natural Science Foundation of China Grant (91939301 to J.-P.S.), Continued Funding of the National Science Fund for Distinguished Young Scholars (82425105 for J.-P.S.), the Key Research Project of the Beijing Natural Science Foundation, China (Z200019 to J.-P.S. and L.T.), National Key R&D Program of China (2018YFC1003600 to X.Y. and J.-P.S., 2022YFA1104003 to Y.X., 2022YFC2702600 to F.Y., 2019YFA0904200 to J.-P.S.), the State Key Program of National Natural Science Foundation of China (32130055 to J.-P.S.), National Natural Science Foundation of China (81773704 to J.-P.S. and 92057121 to X.Y., 82273999 to B.-X.Y., 92168120 to L.T.). National Natural Science Foundation of China Grant (82304601 to S.-M.H. and 82104272 to Y.-L.J.). Open Fund of State Key Laboratory of Vascular Homeostasis and Remodeling (Peking University) (202409, 202410), Major Fundamental Research Program of Natural Science Foundation of Shandong Province, China (ZR2021ZD18 to X.Y.), Shandong Province Key Research and Development Project (2021CXGC011105 to Y.X.). Shandong Taishan Scholar Young Expert (tsqn202408054 to S.-M.H.). The molecular simulations were performed on the HPC Cloud Platform of Shandong

University. The cryo-EM data were collected at the Center of Cryo-Electron Microscopy, Shandong University. We thank Translational Medicine Core Facility of Shandong University and the Cryo-EM Platform of Peking University Health Science Analysis Center for consultation and instrument availability that supported this work.

## Author contributions

J.-P.S., B.-X.Y. organized the project. J.-P.S., B.-X.Y. and L.T. designed and supervised the overall experimental design and execution. X.Y., F.Y., P.X. and Z.Y. provided important discussions and essential revisions. F.Yi. and M.-W.W. provided experimental material for urease detection. M.-Y.X., Y.-H.X. and H. Z. generated the zf-UT, hUT-A2, hUT-A3 and hUT-B insect cell expression construct. S.-M.H., Z.-Z.H., L.L., M.-Y.X., B.-Y.C., K.C. and X.W. prepared samples for cryo-EM. S.-M.H., Z.-Z.H., L.L., M.-Y.X. and B.-Y.C. prepared the cryo-EM grids and collected the cryo-EM data. S.-M.H., J.-L.W., and M.-H.Z. performed cryo-EM map calculation, model building, and structure refinement. Z.-Z.H., M.-Y.X., M.L., B.-Y.C. and C.-H.W. generated zf-UT, hUT-A2, hUT-A3 and hUT-B constructs and mutants for the cell-based assays. Z.-Z.H., M.-Y.X. and Y.-L.J. detected the urea transportation by using C14-labeled urea. S.-M.H. and L.L. detected urea transportation and the effect of inhibitors by using the urease assay kit. C.Z., Z.L. and Y.S. performed molecular dynamics simulations. J.-P.S. and S.-M.H. wrote the initial manuscript. S.-M.H., Z.-Z.H., L.L., M.-Y.X. and B.-Y.C. provided figures.

## Competing interests

The authors declare no competing interests.

## Additional information

**Supplementary information** The online version contains supplementary material available at <https://doi.org/10.1038/s41467-024-54305-y>.

**Correspondence** and requests for materials should be addressed to Lu Tie, Bao-Xue Yang or Jin-Peng Sun.

**Peer review information** *Nature Communications* thanks Gamma Chi, Ming Han, Zhi-Jie Liu, and the other, anonymous, reviewer(s) for their contribution to the peer review of this work. A peer review file is available.

**Reprints and permissions information** is available at <http://www.nature.com/reprints>

**Publisher's note** Springer Nature remains neutral with regard to jurisdictional claims in published maps and institutional affiliations.

**Open Access** This article is licensed under a Creative Commons Attribution-NonCommercial-NoDerivatives 4.0 International License, which permits any non-commercial use, sharing, distribution and reproduction in any medium or format, as long as you give appropriate credit to the original author(s) and the source, provide a link to the Creative Commons licence, and indicate if you modified the licensed material. You do not have permission under this licence to share adapted material derived from this article or parts of it. The images or other third party material in this article are included in the article's Creative Commons licence, unless indicated otherwise in a credit line to the material. If material is not included in the article's Creative Commons licence and your intended use is not permitted by statutory regulation or exceeds the permitted use, you will need to obtain permission directly from the copyright holder. To view a copy of this licence, visit <http://creativecommons.org/licenses/by-nc-nd/4.0/>.

© The Author(s) 2024